The Stereochemistry of *trans*-4-Hydroxynonenal-Derived Exocyclic 1,N^2-2′-Deoxyguanosine Adducts Modulates Formation of Interstrand Cross-Links in the 5′-CpG-3′ Sequence†

Hai Huang,‡ Hao Wang,‡ Nan Qi,‡ R. Stephen Lloyd,§ Carmelo J. Rizzo,‡ and Michael P. Stone*,‡

Department of Chemistry, Center in Molecular Toxicology, Center for Structural Biology and Vanderbilt-Ingram Cancer Center, Vanderbilt University, Nashville, Tennessee 37235, and Center for Research in Occupational and Environmental Toxicology, Oregon Health and Science University, 3181 SW Sam Jackson Park Road, L606, Portland, Oregon 97239-3098

Received June 13, 2008; Revised Manuscript Received August 7, 2008

ABSTRACT: The *trans*-4-hydroxynonenal (HNE)-derived exocyclic 1,N^2-dG adduct with (6*S*,8*R*,11*S*) stereochemistry forms interstrand N^2-dG−N^2-dG cross-links in the 5′-CpG-3′ DNA sequence context, but the corresponding adduct possessing (6*R*,8*S*,11*R*) stereochemistry does not. Both exist primarily as diastereomeric cyclic hemiacetals when placed into duplex DNA [Huang, H., Wang, H., Qi, N., Kozekova, A., Rizzo, C. J., and Stone, M. P. (2008) *J. Am. Chem. Soc. 130*, 10898−10906]. To explore the structural basis for this difference, the HNE-derived diastereomeric (6*S*,8*R*,11*S*) and (6*R*,8*S*,11*R*) cyclic hemiacetals were examined with respect to conformation when incorporated into 5′-d(GCTAGCXAGTCC)-3′•5′-d(GGACTCGCTAGC)-3′, containing the 5′-CpX-3′ sequence [X = (6*S*,8*R*,11*S*)- or (6*R*,8*S*,11*R*)-HNE−dG]. At neutral pH, both adducts exhibited minimal structural perturbations to the DNA duplex that were localized to the site of the adduction at X^7•C^{18} and its neighboring base pair, A^8•T^{17}. Both the (6*S*,8*R*,11*S*) and (6*R*,8*S*,11*R*) cyclic hemiacetals were located within the minor groove of the duplex. However, the respective orientations of the two cyclic hemiacetals within the minor groove were dependent upon (6*S*) versus (6*R*) stereochemistry. The (6*S*,8*R*,11*S*) cyclic hemiacetal was oriented in the 5′-direction, while the (6*R*,8*S*,11*R*) cyclic hemiacetal was oriented in the 3′-direction. These cyclic hemiacetals effectively mask the reactive aldehydes necessary for initiation of interstrand cross-link formation. From the refined structures of the two cyclic hemiacetals, the conformations of the corresponding diastereomeric aldehydes were predicted, using molecular mechanics calculations. Potential energy minimizations of the duplexes containing the two diastereomeric aldehydes predicted that the (6*S*,8*R*,11*S*) aldehyde was oriented in the 5′-direction while the (6*R*,8*S*,11*R*) aldehyde was oriented in the 3′-direction. These stereochemical differences in orientation suggest a kinetic basis that explains, in part, why the (6*S*,8*R*,11*S*) stereoisomer forms interchain cross-links in the 5′-CpG-3′ sequence whereas the (6*R*,8*S*,11*R*) stereoisomer does not.

trans-4-Hydroxynonenal (**1**, HNE)[1] is produced from the metabolism of membrane lipids (*1*), and it is the major in vivo peroxidation product of ω-6 polyunsaturated fatty acids (*2, 3*). Several routes for the formation of HNE from ω-6 polyunsaturated fatty acids have been described (*4–6*). HNE exhibits a range of biological effects, from alteration in gene expression and cell signaling to cell proliferation and apoptosis (*7–13*). Human exposures to HNE have been implicated in the etiologies of a number of diseases associated with oxidative stress, including Alzheimer's disease (*14*), Parkinson's disease (*15*), arteriosclerosis (*16*), and hepatic ischemia reperfusion injury (*17*).

With regard to genotoxicity, HNE induces the SOS response in *Escherichia coli* (*18*). Chromosomal aberrations were observed upon exposures to HNE in rodent (*19, 20*), mammalian (*21, 22*), and human (*23*) cells. In mammalian cells, the genotoxicity of HNE depends upon glutathione levels that modulate the formation of HNE−DNA adducts (*24–26*). Michael addition of the N^2-amino group of 2′-deoxyguanosine to HNE gives four diastereomeric exocyclic 1,N^2-dG adducts **2**−**5** (*27–29*) that have been detected in cellular DNA (*30–36*). Alternatively, oxidation of HNE to 2,3-epoxy-4-hydroxynonanal and further reaction with nucleobases afford etheno adducts (*37–41*).

The mutational spectrum induced by HNE−dDNA adducts in the *lacZ* gene of the single-stranded M13 phage transfected into wild-type *E. coli* revealed recombination events, C → T transitions, followed by G → C and A → C transversions, and frameshift mutations (*29*). HNE is mutagenic (*42*) and

† This work was supported by NIH Grant ES-05355 (R.S.L., C.J.R., and M.P.S.). Funding for the NMR spectrometers was supplied by Vanderbilt University, by NIH Grant RR-05805, and by the Vanderbilt Center in Molecular Toxicology (ES-00267). The Vanderbilt-Ingram Cancer Center is supported by NIH Grant CA-68485.

* To whom correspondence should be addressed. E-mail: michael.p.stone@vanderbilt.edu. Phone: (615) 322-2589. Fax: (615) 322-7591.

‡ Vanderbilt University.

§ Oregon Health and Science University.

[1] Abbreviations: HNE, *trans*-4-hydroxynonenal; HNE−dG, *trans*-4-hydroxynonenal-derived 2′-deoxyguanosine adduct; NOE, nuclear Overhauser effect; NOESY, nuclear Overhauser effect spectroscopy; COSY, correlation spectroscopy; DQF-COSY, double-quantum-filtered correlation spectroscopy; TOCSY, total correlation spectroscopy; rMD, restrained molecular dynamics; rmsd, root-mean-square deviation.

10.1021/bi8011143 CCC: $40.75
Published on Web 10/11/2008

carcinogenic in rodent cells (*43*). Hussain et al. (*44*) reported that HNE caused G•C → T•A transversions at codon 249 of wild-type *p53* in lymphoblastoid cells. Hu et al. (*45*) further reported that HNE−DNA adducts were preferentially formed with guanine at the third base of codon 249 in the *p53* gene. The mutational spectrum induced by HNE−dDNA adducts in the *supF* gene of shuttle vector pSP189 replicated in human cells showed that HNE induced primarily G → T transversions, accompanied by lower levels of G → A transitions (*46*). Fernandes et al. (*47*) conducted site-specific mutagenesis studies and observed that in the 5′-CpG-3′ duplex of interest in this work, only stereoisomers **2** and **3** of the HNE-induced exocyclic 1,N^2-dG adduct were mutagenic, inducing low levels of G → T transversions and G → A transitions (*47*). Evidence that the nucleotide excision repair pathway is involved in the repair of HNE−dG lesions has been obtained (*46, 48, 49*).

Wang et al. (*50, 51*) synthesized the four stereoisomers of the exocyclic 1,N^2-dG adduct (**2**−**5**) and incorporated them into the 5′-CpG-3′ sequence context of 5′-d(GCTAGCX-AGTCC)-3′•5′-d(GGACTCGCTAGC)-3′, in which X denotes the HNE−dG adduct. The related 2′-deoxyguanosine adducts of acrolein (*52–55*) and crotonaldehyde (*56*) formed reversible interchain cross-links in this sequence context (*57*). DNA interstrand cross-links block DNA replication and transcription, resulting in cell death if the lesion is not repaired (*58*). At equilibrium, the (6*R*) stereoisomer of the crotonaldehyde adduct reached cross-linking levels of 38% as compared to only 5% for the (6*S*) stereoisomer (*53*). Similarly, of the four HNE−dG adducts, only stereoisomer **3** possessing (6*S*,8*R*,11*S*) stereochemistry resulted in the formation of DNA reversible interchain cross-links. DNA cross-linking by (6*S*,8*R*,11*S*) stereoisomer **3** represented the predominant species present (>85%) when chemical equilibrium was attained, suggesting that this cross-link is particularly stable in duplex DNA (*51*). Significantly, this HNE isomer possessed the same relative stereochemistry as the (6*R*) crotonaldehyde adduct. However, cross-link formation was slow, with chemical equilibrium being attained only after several months at room temperature (*51*). The discovery that diastereomeric HNE−dG adducts **2** and **3** exist primarily as cyclic hemiacetals **8**−**11** when placed into duplex DNA provided a rationale for the slow rate of interstrand cross-link formation by stereoisomer **3** (*59*). This has also been observed for the Michael addition of protein nucleophiles to HNE (*60*). The presence of the hemiacetal effectively masks the reactive aldehyde species necessary for cross-link formation. Kurtz and Lloyd (*61*) demonstrated that HNE adduct **3** formed conjugates with the tetrapeptide KWKK more rapidly than did the other three stereoisomeric HNE adducts, **2**, **4**, and **5**.

In this work, the cyclic hemiacetal rearrangement products **8** and **10** of the HNE-derived exocyclic 1,N^2-dG adducts with (6*R*,8*S*,11*R*) and (6*S*,8*R*,11*S*) stereochemistry (*59*) were examined with respect to the structure in 5′-d(GCTAGCX-AGTCC)-3′•5′-d(GGACTCGCTAGC)-3′, containing the 5′-CpX-3′ sequence (X = HNE−dG), using high field NMR. Both of these stereoisomeric hemiacetals exhibited minimal structural perturbation of the DNA duplex, which in both instances was localized to the site of the adduction at X^7•C^{18} and its neighboring base pair, A^8•T^{17}. Both stereoisomeric cyclic hemiacetals were oriented in the minor groove of the DNA duplex. However, the orientations of the cyclic hemiacetals were different for the two stereoisomers. The cyclic hemiacetal **10** derived from the (6*S*,8*R*,11*S*) HNE adduct **3** was oriented in the 5′-direction, while the cyclic hemiacetal **8** derived from the (6*R*,8*S*,11*R*) HNE adduct **2** was oriented in the 3′-direction. Cyclic hemiacetals **8** and **10** represent surrogates for reactive aldehydes **6** and **7** that mediate DNA interstrand cross-linking. From the refined structures of the two cyclic hemiacetals **8** and **10**, the conformations of the corresponding diastereomeric aldehydes **6** and **7** were predicted, based upon molecular mechanics calculations. Potential energy minimizations of the DNA duplexes containing the two diastereomeric aldehydes **6** and **7** were consistent with the prediction that the (6*R*) aldehyde **6** was oriented in the 3′-direction while the (6*S*) aldehyde **7** was oriented in the 5′-direction. These differences in minor groove orientation suggest a kinetic basis for explaining, in part, the relative abilities of the (6*S*,8*R*,11*S*) and (6*R*,8*S*,11*R*) diastereomeric adducts **2** and **3** to form interchain cross-links in the 5′-CpG-3′ sequence (*51*).

MATERIALS AND METHODS

Materials. The oligodeoxynucleotide 5′-d(GGACTCGC-TAGC)-3′ was synthesized and purified by anion-exchange chromatography by the Midland Certified Reagent Co. (Midland, TX). The HNE-derived (6*R*,8*S*,11*R*) and (6*S*,8*R*,11*S*) exocyclic 1,N^2-2′-deoxyguanosine adducts **2** and **3** [which rearrange predominately to **8** and **10** in duplex DNA, respectively (*59*)] were incorporated into 5′-d(GCTAGCX-AGTCC)-3′ (X = HNE−dG) as reported previously (*50, 51*). The oligodeoxynucleotides were characterized by MALDI-TOF mass spectrometry. Capillary gel electrophoresis and C-18 HPLC were utilized to assess their purities. The oligodeoxynucleotides were desalted by chromatography on Sephadex G-25 (Sigma-Aldrich, St. Louis, MO). The concentrations of the oligodeoxynucleotides were determined by UV absorption at 260 nm, and the extinction coefficients of both sequences were calculated to be 1.12×10^5 L mol^{-1} cm^{-1} (*62*). The strands were annealed at a 1:1 stoichiometry in 10 mM NaH_2PO_4, 100 mM NaCl, and 50 μM Na_2EDTA (pH 7.0). The solutions were heated to 95 °C for 10 min and then cooled to room temperature. The duplex DNA was purified using DNA grade hydroxylapatite chromatography, with a gradient from 10 to 200 mM NaH_2PO_4 in 100 mM NaCl and 50 μM Na_2EDTA (pH 7.0), and desalted using Sephadex G-25. The duplexes were also characterized by MALDI-TOF mass spectrometry.

NMR Experiments. NMR experiments were performed at ^{1}H frequencies of 600 and 800 MHz; the data at 800 MHz were collected using a cryogenic probe. Samples were at a strand concentration of 1.0 mM. Samples for the nonexchangeable protons were dissolved in 10 mM NaH_2PO_4, 100 mM NaCl, and 50 μM Na_2EDTA (pH 7.0) to a volume of 280 μL. They were exchanged with D_2O and suspended in 280 μL of 99.996% D_2O. The pH was adjusted using dilute DCl or NaOD. The temperature was 25 °C. Samples for the observation of exchangeable protons were dissolved in 280 μL of the same buffer containing a 9:1 H_2O/D_2O mixture (v/v). The temperature was 5 °C. The ^{1}H chemical shifts were referenced to water. Data were processed using FELIX 2000 (Accelrys Inc., San Diego, CA) on LINUX workstations

(Dell Inc., Austin, TX). For all experiments, a relaxation delay of 1.5 s was used. The NOESY spectra were recorded with 512 real data in the t_2 dimension and 2048 real data in the t_1 dimension. The spectra were zero-filled during processing to create a matrix of 1024 × 1024 real points. The TOCSY mixing time was 80 ms for stereoisomer **8** and 100 ms for stereoisomer **10**. TOCSY spectra were zero-filled to create a matrix of 1024 × 512 real points. For assignment of exchangeable protons, NOESY experiments used the Watergate solvent suppression scheme (*63*). The mixing time was 250 ms. For assignment of nonexchangeable protons and the derivation of distance restraints, NOESY experiments used TPPI quadrature detection, and mixing times of 60, 150, 200, and 250 ms were used. The DQF-COSY experiments were performed with TPPI quadrature detection and presaturation of the residual water during the relaxation delay. ^{1}H−^{31}P HMBC spectra (*64, 65*) were recorded at 30 °C. The data matrix consisted of 96 (t_1) × 1024 (t_2) complex points. The data were Fourier-transformed after zero filling in the t_1 dimension, resulting in a matrix size of 128 (D_1) × 512 (D_2) real points. The ^{31}P chemical shifts were not calibrated.

Experimental Distance and Torsion Angle Restraints. Footprints were drawn around cross-peaks obtained with a mixing time of 250 ms using FELIX 2000. Identical footprints were transferred and fit to the corresponding cross-peaks obtained at the other two mixing times. Cross-peak intensities were determined by volume integrations. These were combined as necessary with intensities generated from complete relaxation matrix analysis of a starting structure to generate a hybrid intensity matrix (*66, 67*). MARDIGRAS (*68–70*) iteratively refined the hybrid intensity matrix and optimized agreement between calculated and experimental NOE intensities. The RANDMARDI algorithm carried out 50 iterations for each set of data, randomizing peak volumes within limits specified by the input noise level (*70*). Calculations were initiated using isotropic correlation times of 2, 3, and 4 ns, and with both A-form and B-form starting structures and the three mixing times, yielding 18 sets of distances. Analysis of these data yielded experimental distance restraints used in subsequent rMD calculations, and the corresponding standard deviations for the distance restraints.

The 2-deoxyribose pseudorotational angles (P) were estimated by examining the $^3J_{HH}$ values of sugar protons (*71*). $J_{1'-2'}$ and $J_{1'-2''}$ were measured from ECOSY spectra, while the intensities of H2″−H3′ and H3′−H4′ cross-peaks were determined from DQF-COSY spectra. The data were fit to curves relating the coupling constants to the 2-deoxyribose pseudorotation (P), the sugar pucker amplitude (ϕ), and the percentage of S-type conformation. The pseudorotation and amplitude ranges were converted to the five dihedral angles ν_0−ν_4. Coupling constants measured from ^{1}H−^{31}P HMBC spectra were applied (*72, 73*) to the Karplus relationship (*74*) to determine the backbone dihedral angle ε (C4′−**C3′**−**O3′**−P), related to the H3′−**C3′**−**O3′**−P angle by a 120° shift. The ζ (C3′−**O3′**−**P**−O5′) backbone angles were calculated from the correlation between ε and ζ in B-DNA.

rMD Calculations. The HNE-adducted duplexes, in either A-form or B-form DNA helical coordinates, were constructed by bonding the stereospecific cyclic hemiacetal forms of the HNE adducts (*59*) to N^2 of G^7 using Insight II. The partial charges on the cyclic hemiacetal form of the HNE−dG adduct were obtained from density functional theory (DFT) calculations using a neutral total charge, utilizing the B3LYP/6-31G* basis set and GAUSSIAN (*75*). To obtain the A-form and B-form starting structures that were used for subsequent restrained molecular dynamics (rMD) calculations, these A-form or B-form modified duplexes were energy-minimized using 200 iterations with the conjugate gradient algorithm, in the absence of experimental restraints.

Distance restraints were divided into classes weighted according to the error assessed in their measurements. Class 1, class 2, class 3, class 4, and class 5 were calculated from completely resolved, somewhat overlapped, slightly overlapped, intermediately overlapped, or heavily overlapped cross-peaks, respectively, which were at least 0.5 ppm from the water resonance or the diagonal line of the spectrum. Class 5 also included all other cross-peaks. NOEs that did not have a distance calculated by MARDIGRAS were estimated by relative peak intensities. The spectroscopic data indicated that the duplexes conserved Watson−Crick base pairing, so empirical restraints preserving Watson−Crick hydrogen bonding and preventing propeller twisting between base pairs were used (*76*). Empirical backbone and 2-deoxyribose torsion angle restraints derived from B-DNA were used (*77*). The potential energy wells associated with the dihedral angle restraints were ±30°. The force constants of the restraints were scaled from 3.2 to 32 kcal mol^{-1} Å^{-2} during the first 10 ps and were maintained at 32 kcal mol^{-1} Å^{-2} for the remainder of the simulations.

Ten sets of randomly seeded rMD calculations (five from A-type and five from B-type DNA starting structures) were conducted using AMBER (version 7.0) (*78*) and the parm99 force field. The Hawkins, Cramer, Truhlar pairwise generalized Born (GB) model (*79, 80*) was used to simulate implicit waters. The parameters developed by Tsui and Case (*81*) were used. The cutoff radius for nonbonding interactions was 18 Å. The restraint energy function contained terms describing distance and torsion angle restraints, both in the form of square well potentials. Bond lengths involving hydrogens were fixed with the SHAKE algorithm (*82*). A 1000-step energy minimization was performed with an integrator time of 1 fs without experimental restraints, followed by a 100000-iteration simulated annealing protocol with an integrator time step of 1 fs. The system was heated to 600 K in 5000 iterations, kept at 600 K for 5000 iterations, and then cooled to 100 K with a time constant of 4.0 ps over 80000 iterations. A final cooling was applied to relax the system to 0 K with a time constant of 1.0 ps over 10000 iterations.

Convergence was assessed for structures having the fewest deviations from the experimental distance and dihedral restraints, the lowest van der Vaals energies, and the lowest overall energies. Finally, the 10 refined structures were energy-minimized for 250 iterations without restraints to yield average structures. CORMA (*67*) was utilized to calculate the predicted NOE intensities from the structures refined from rMD calculations. Input volumes (intensities) were normalized from the intensities of protons with fixed intranuclear distances (i.e., cytosine H5−H6 and thymine CH_3−H6 distances). Random noise was added to all intensities to simulate spectral noise. An isotropic correlation time (τ_c) of 3 ns was used. The rotation of thymidine CH_3 groups was modeled using a three-jump site model (*83*). A sixth-

Chart 1: Formation of Exocyclic 1,N^2-dG Adducts by HNE

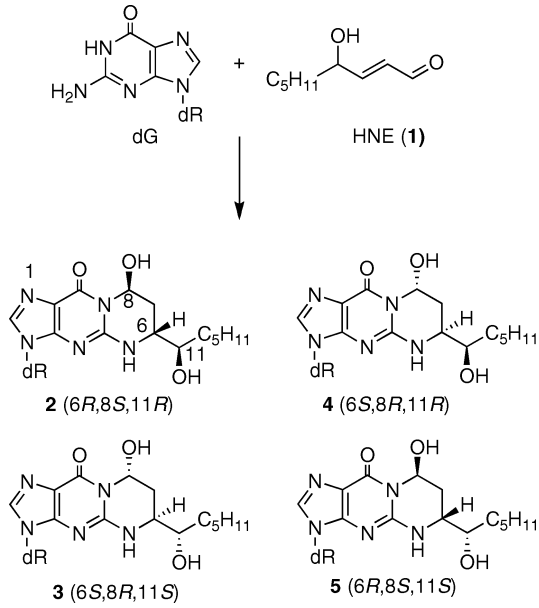

root residual (R_1^x) factor (*84*) was calculated for each structure. Helicoidal analysis was carried out with 3DNA (*85*).

Molecular Modeling. The starting structures were created from the refined structures of the duplexes containing cyclic hemiacetal **8** or **10**, using INSIGHT II. The partial charges of aldehydes **6** and **7** arising from HNE−dG adducts **2** and **3** were obtained from density functional theory (DFT) calculations using a neutral total charge, utilizing the B3LYP/6-31G* basis set and GAUSSIAN (*75*). Potential energy minimization calculations were conducted with AMBER (version 7.0) (*78*) and the parm99 force field. The pairwise generalized Born (GB) model (*79, 80*) was used to simulate implicit waters. The parameters developed by Tsui and Case (*81*) were used. The cutoff radius for nonbonding interactions was 18 Å. A 1000-iteration potential energy minimization was performed, using the conjugate gradient algorithm.

RESULTS

*NMR Characterization of HNE-Derived Exocyclic 1,N^2-dG Adducts **2** and **3**.* The Watson−Crick face of the exocyclic 1,N^2-dG adducts arising from HNE is blocked, thereby preventing base pairing with dC. Analyses of NMR data (*59*) indicated that when either exocyclic adduct **2** or **3** (Charts 1 and 2) was placed into duplex DNA opposite cytosine, ring opening to aldehydes occurred. However, in contrast to the corresponding acrolein-derived (*86*) and crotonaldehyde-derived exocyclic 1,N^2-dG (*56*) adducts, the major forms of the ring-opened species derived from HNE adduct **2** or **3** were not aldehydes when at equilibrium in duplex DNA. Mass spectrometric analyses of oligodeoxynucleotides containing **2** and **3** indicated that they were not hydrates of the aldehyde, but rather diastereomeric sets of cyclic hemiacetals **8** and **9** or **10** and **11** (Chart 3), arising from HNE adduct **2** or **3**, respectively (*59*). In each instance, NMR indicated that the H6 and H8 HNE protons preferred the *trans* configuration, which in both cases, was presumably driven by steric repulsion from the large substituent groups. Thus, when one starts from adduct **2**, cyclic hemiacetal stereoisomer **8** (6*R*,8*S*,11*R*) is the major species at equilibrium and stereoisomer **9** (6*R*,8*R*,11*R*) is the minor species. Likewise, when one starts from adduct **3**, cyclic hemiacetal stereoisomer **10** (6*S*,8*R*,11S) is the major species and stereoisomer **11** (6*S*,8*S*,11*S*) is the minor species (*59*). Therefore, these results detail the conformational analyses of cyclic hemiacetal stereoisomers **8** and **10**, representing the major species present in the samples of duplex DNA, at equilibrium.

*Duplex Containing (6R,8S,11R) HNE-Derived Cyclic Hemiacetal Adduct **8**. (a) Nonexchangeable Protons.* The sequential NOE assignment was accomplished using standard protocols (*87, 88*). The sequential NOEs between the aromatic and anomeric protons are displayed in panels A and B of Figure 1. The spectral resolution of this modified duplex was challenging because of a large number of pyrimidine aromatic resonances, e.g., T^3 H6, T^{17} H6, C^{18} H6, C^{20} H6, T^{21} H6, and C^{24} H6, resonating between 7.35 and 7.45 ppm. Nevertheless, for the modified strand, a complete sequential NOE connectivity was observed. For the complementary strand, the C^{18} H1′ and T^{17} H1′ resonances were superimposed, with C^{18} being the nucleotide complementary to X^7. The geminal 2-deoxyribose proton resonances were assigned by utilizing a combination of DQF-COSY and NOESY spectra, based upon the expectation that the H2″ protons were located further downfield (*87, 88*). With the exception of several of the H4′ protons, and the stereotopic assignments of the H5′ and H5″ sugar protons, assignments were made unequivocally. In general, canonical B-DNA distances between the H4′, H5′, and H5″ protons were used to tentatively assign the H5′ and H5″ 2-deoxyribose protons. The assignments of the nonexchangeable protons are provided in Table S1 of the Supporting Information.

(b) Exchangeable Protons. A plot of the region ranging from 12.0 to 14.4 ppm of the NOESY specrtum is shown in Figure 2A. The imino proton resonances were assigned following standard protocols (*89*). The X^7 N9H → C^{18} N^4H(s) NOEs were observed, indicating the presence of the X^7•C^{18} pair at the modification site (Figure 3A). A strong NOE cross-peak was observed between the guanine imino proton at the modified base, X^7 N9H, and the guanine amino proton at the modified base, X^7 N5H. This was also consistent with Watson−Crick base pairing at the adduct site. NOE correlations of some HNE protons with X^7 N9H, X^7 N5H, and G^{19} N1H were observed (Figure 3A). The X^7 N9H → A^8 H2 NOE was also observed, consistent with the intrahelical stacking of the modified nucleotide X^7 (Figure 3A). A complete NOE connectivity was obtained, with the exceptions of terminal base pairs G^1•C^{24} and C^{12}•G^{13}, the imino resonances of which were broadened by solvent exchange.

(c) HNE Protons. In the DQF-COSY spectrum, a resonance observed at 5.45 ppm exhibited both dipolar and scalar couplings to a resonance observed at 2.13 ppm (Figure 4A). This was assigned as a correlation between X^7 H8 and the geminal X^7 $H7^{\alpha}$ proton. Another resonance, observed at 3.93 ppm, exhibited scalar coupling to a resonance observed at 2.15 ppm and was assigned as a correlation between X^7 H6 and the X^7 $H7^{\beta}$ proton. These assignments were corroborated by NOESY data obtained with a mixing time of 60 ms. The difference in the chemical shifts of the two geminal X^7 H7 protons was <0.02 ppm. Both X^7 H7 protons exhibited NOE

Chart 2: Ring-Opening Chemistry of the HNE-Derived Exocyclic 1,N^2-dG Adducts When Placed Opposite dC in Duplex DNA

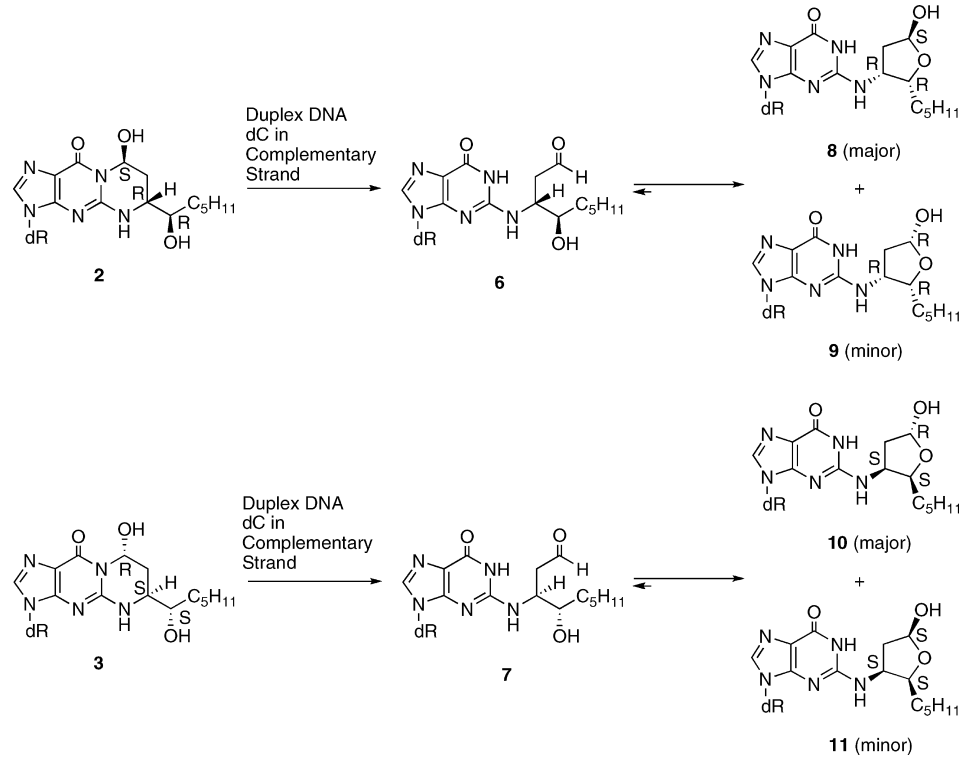

Chart 3: (A) Numbering Scheme of the 5′-CpG-3′ Duplexes Containing Stereospecific HNE−dG Adducts and (B) Numbering Scheme of the HNE−dG Adducts

A

5'-G^1 C^2 T^3 A^4 G^5 C^6 X^7 A^8 G^9 $T^{10}C^{11}C^{12}$-3'
3'-$C^{24}G^{23}A^{22}T^{21}C^{20}G^{19}C^{18}T^{17}C^{16}A^{15}G^{14}G^{13}$-5'

B

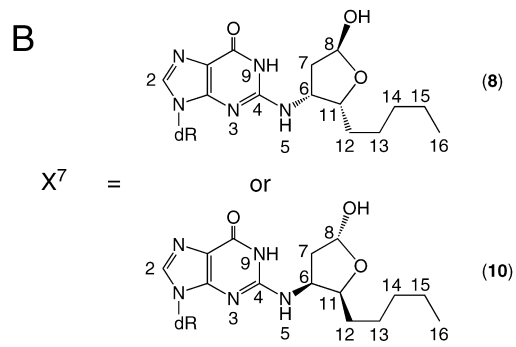

cross-peaks with X^7 H6 and X^7 H8. The X^7 H6 → X^7 H11 and X^7 H11 → X^7 H12(s) correlations, observed in both NOESY and DQF-COSY spectra, were used to assign the resonances of the X^7 H11 and X^7 H12 protons. The resonances of X^7 H12−H16 overlapped. Both H7 protons exhibited strong NOE cross-peaks with H8 and H6. The H6 → $H7^{\alpha}$ correlation was stronger than the H6 → $H7^{\beta}$ correlation, while the $H7^{\alpha}$ → H8 correlation was weaker than the $H7^{\beta}$ → H8 correlation. X^7 H6 also exhibited a correlation with X^7 H11 in both the NOESY and COSY spectra.

The X^7 H11 → X^7 H12 correlations in the COSY and NOESY spectra were used to assign X^7 H12 protons. The X^7 H16 protons were the most upfield; they exhibited correlations with X^7 H15 in the COSY and NOESY spectra. The chemical shifts of the geminal H12, H13, H14, and H15 protons were similar. The resonances and NOE cross-peaks of X^7 H13 and H14 were assigned using an iterative strategy. NOE peaks associated with the H6, H7, H8, H11, and H16 protons were assigned and converted to distance restraints; rMD calculation then provided a preliminary structure, which was used to evaluate other unassigned NOEs. The final NOE assignments were made following several rounds of iteration. The chemical shifts of the HNE protons and the assigned NOEs are listed in Table 1.

(d) Chemical Shift Perturbations. The chemical shift perturbations of the nonexchangeable pyrimidine H6, purine H8, and 2-deoxyribose H1′ protons, comparing the modified and the corresponding unmodified duplexes, are presented in panels A and B of Figure 5. Large differences were observed at the adducted base pair X^7•C^{18}. As compared to the X^7 and C^{18} 2-deoxyribose H1′ protons in the unmodified duplex, in the modified duplex, these H1′ resonances shifted downfield 0.32 and 0.41 ppm, respectively. Few chemical shift perturbations were observed for the pyrimidine H6 and purine H8 protons, indicating that the DNA duplex was minimally disturbed by the presence of the HNE-derived cyclic hemiacetal.

(e) NMR-Derived Distances. A total of 89 NOE cross-peaks associated with the protons of the cyclic hemiacetal moiety protons were assigned (Table 1). Figure 6A shows some of these correlations. Notably, NOE correlations were observed between the geminal X^7 H7 as well as X^7 H6 protons and A^8 H2 and A^8 H1′ protons that were in the 3′-direction. In contrast, the G^{19} H1′ and C^{20} H1′ protons that were in the 5′-direction exhibited NOE cross-peaks with the X^7 H12−H15 protons. These findings suggested that the cyclic hemiacetal moiety was located in the minor groove with the tetrahydrofuran oriented in the 3′-direction and the aliphatic chain oriented in the 5′-direction.

(f) 2-Deoxyribose and Backbone Angle Conformations. The 2-deoxyribose and backbone angle conformations were

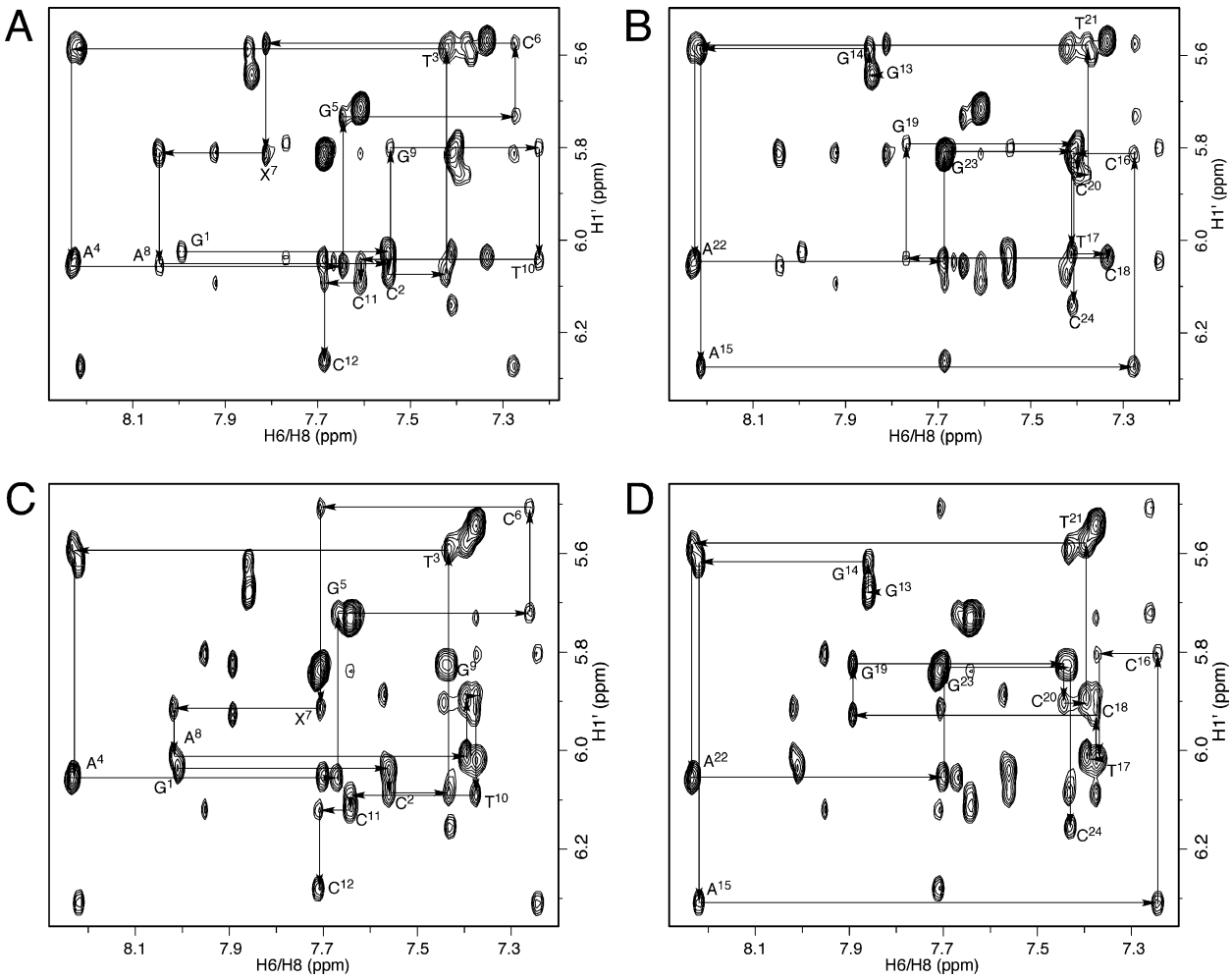

FIGURE 1: Expansion of the NOESY spectra for the oligodeoxynucleotide duplexes containing the 5′-CpX-3′ sequence, showing correlations of purine H8 and pyrimidine H6 protons with 2-deoxyribose H1′ protons. (A) Modified strand of the duplex adducted with cyclic hemiacetal **8**. (B) Complementary strand of the duplex adducted with cyclic hemiacetal **8**. (C) Modified strand of the duplex adducted with cyclic hemiacetal **10**. (D) Complementary strand of the duplex adducted with cyclic hemiacetal **10**.

determined spectroscopically from DQF-COSY and ^{31}P−H3′ HMBC correlations. Evaluation of the DQF-COSY spectrum revealed that the 2-deoxyribose pseudorotations for all nucleotides were either $C_{1'}$-*exo* or $C_{2'}$-*endo*.

(g) Structure Refinement. The structural refinement involved 527 distance restraints, including 296 intraresidue and 231 interresidue restraints, obtained from the intensities of NOE cross-peaks. In addition, 52 empirical distance restraints defining Watson−Crick base pairing were used to refine the structure of the duplex; their use was predicated upon inspection of the NMR data, which indicated that Watson−Crick base pairing was intact throughout the duplex. Finally, an additional 200 empirical backbone torsion angle restraints were also used for structure refinements; these were based upon inspection of the NMR data, which suggested that the adducted duplex maintained a B-type architecture (Table 2).

The randomly seeded rMD calculations were performed starting with initial structures, which were created with either A- or B-form geometries. Pairwise rmsd analysis of emergent structures indicated that the calculations converged, irrespective of starting structure (Table 2). The accuracies of the emergent structures were evaluated by comparison of theoretical NOE intensities calculated by complete relaxation analysis for the refined structure to the experimental NOE intensities, which yielded sixth-root residuals (R_1^x). This residual was less than 0.1 for the modified duplex (Table 2), and the inter- and intranucleotide residuals for individual nucleotides were less than 0.15 (Figure 7A,B), indicating that the refined structures provided an accurate depiction of the data.

(h) Analysis of rMD Structures. The refined structures are overlaid in Figure 8A, and an expanded view of the adducted region of the average structure is shown in Figure 9A. The modified duplex maintained B-type DNA geometry. All nucleotides maintained the *anti* conformation about the glycosyl torsion angle. Few torsion angle differences were observed as compared to ideal B-DNA. The 2-deoxyribose pseudorotations were consistently either $C_{1'}$-exo or $C_{2'}$-endo. The HNE-derived cyclic hemiacetal moiety was folded in the minor groove. The tetrahydrofuran was oriented in the 3′-direction, and the aliphatic chain was oriented in the 5′-direction. Panels A and B of Figure 10 show the base stacking of the adduct region.

Molecular Modeling of the Duplex Containing (6R,8S,11R) HNE-Derived Aldehydic Adduct ***6.*** The refined structure of the cyclic hemiacetal **8** was then converted to the corresponding aldehyde **6** that represents the reactive species necessary for DNA cross-link formation. At equilibrium, this species was not present in sufficient quantity to enable detailed structural refinement. Consequently, a molecular

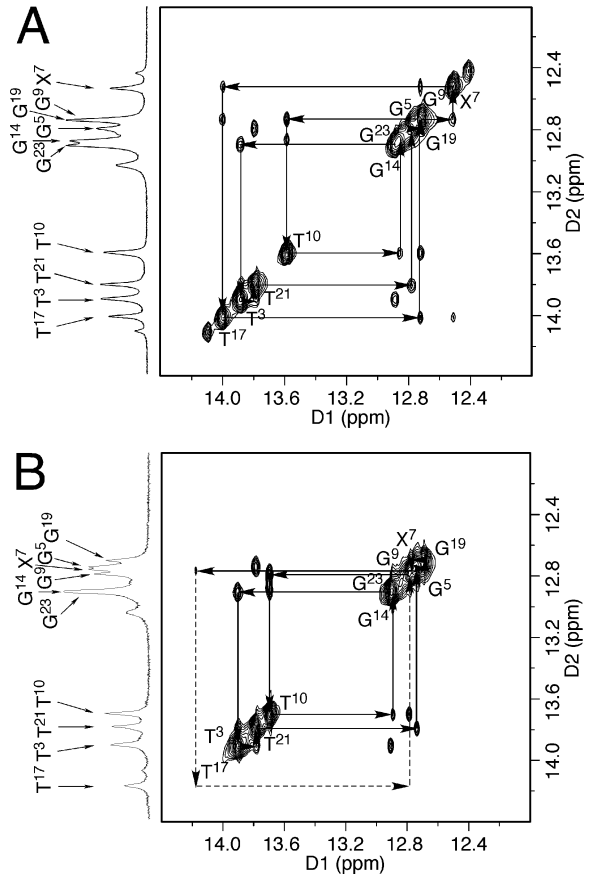

FIGURE 2: Expansions of NOESY spectra for oligodeoxynucleotide duplexes containing the 5′-CpX-3′ sequence, showing the sequential connectivity of the base imino protons. (A) Duplex adducted with cyclic hemiacetal **8**. (B) Duplex adducted with cyclic hemiacetal **10**. The T^{17} N3H resonance for the duplex containing cyclic hemiacetal **10** is broad. It exhibits a weak NOE cross-peak with X^7 N9H, but the diagonal peak is missing.

mechanics approach, using potential energy minimization, was employed to predict the conformation of aldehyde **6** in the minor groove of the DNA duplex. Figure 9B shows the predicted structure of the duplex containing aldehyde **6**, with the HNE moiety remaining in the minor groove, and the aldehyde group oriented in the 3′-direction.

*Duplex Containing (6S,8R,11S) HNE-Derived Cyclic Hemiacetal Adduct **10**. (a) Nonexchangeable Protons.* The resonances of the nonexchangeable protons were assigned using standard approaches (*87, 88*). The sequential NOEs between the aromatic and anomeric protons are displayed in panels C and D of Figure 1. Similar to that of the duplex containing adduct **8**, a complete sequential NOE connectivity was observed. For the complementary strand, a complete sequential NOE connectivity was also observed. The 2-deoxyribose sugar proton resonances were assigned by utilizing a combination of DQF-COSY and NOESY spectra. Compared with the H2′ protons, the geminal H2″ protons are located downfield (*87, 88*). With the exception of several of the H4′ protons, and the stereotopic assignments of the H5′ and H5″ sugar protons, assignments were made unequivocally. In general, canonical B-DNA distances between the H4′, H5′, and H5″ protons were used to tentatively assign the H5′ and H5″ 2-deoxyribose protons. The assignments of the nonexchangeable protons are provided in Table S1 of the Supporting Information.

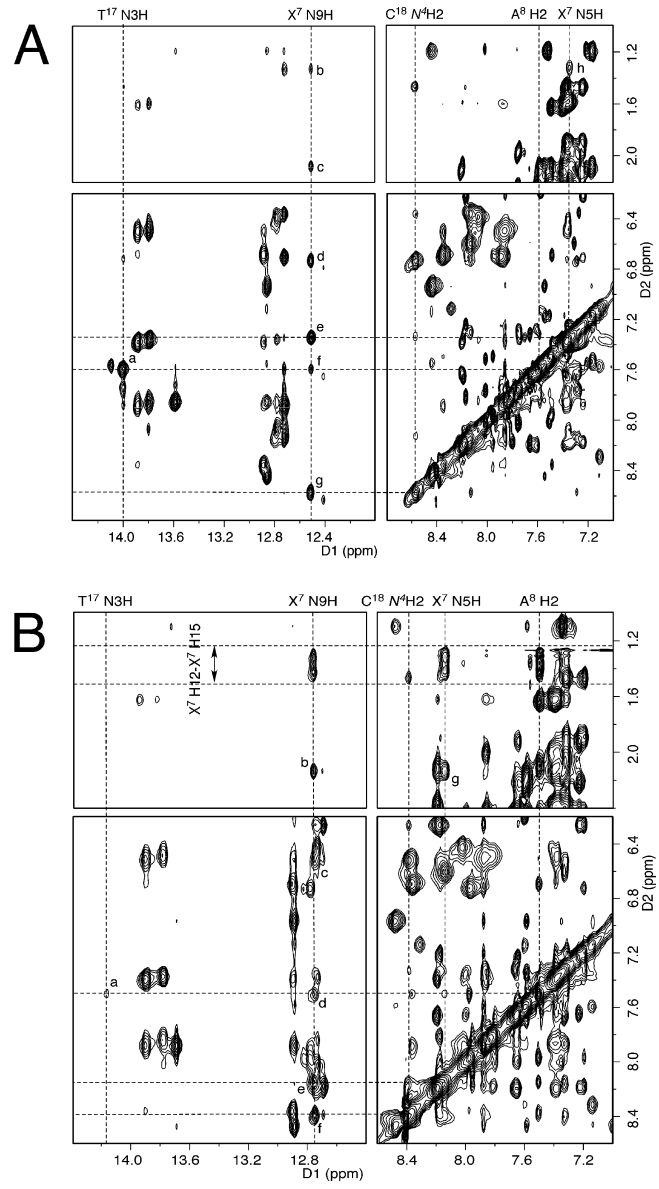

FIGURE 3: Expansions of the NOESY spectra for oligodeoxynucleotide duplexes containing the 5′-CpX-3′ sequence, showing the conservation of Watson−Crick base pairing. (A) Duplex containing cyclic hemiacetal **8**. The NOE cross-peaks were assigned as follows: (a) T^{17} N3H → A^8 H2, (b) X^7 N9H → X^7 H12$^\alpha$, (c) X^7 N9H → X^7 H7$^\alpha$, (d) X^7 N9H → C^{18} N^4H1, (e) X^7 N9H → X^7 N5H, (f) X^7 N9H → A^8 H2, (g) X^7 N9H → C^{18} N^4H2, and (h) X^7 N5H → X^7 H12$^\alpha$. (B) Duplex containing cyclic hemiacetal **10**. The NOE cross-peaks were assigned as follows: (a) T^{17} N3H → A^8 H2, (b) X^7 N9H → X^7 H7, (c) X^7 N9H → C^{18} N^4H1, (d) X^7 N9H → A^8 H2, (e) X^7 N9H → X^7 N5H, (f) X^7 N9H → C^{18} N^4H2, and (g) X^7 N5H → X^7 H7. The two dashed lines indicated by an arrow at the top of the spectrum represent the X^7 H12, H13, H14, and H15 resonances, which could not be assigned unequivocally. They exhibit NOE correlations with X^7 N9H, X^7 N5H, and A^8 H2.

(b) Exchangeable Protons. Figure 2B shows the region of the NOESY spectrum showing the NOEs between the imino protons. The T^{17} N3H imino proton appeared as a broad peak at 14.2 ppm; it exhibited a weak cross-peak with the X^7 N9H imino proton. This assignment was supported by observation of an NOE cross-peak to A^8 H2 (Figure 3B). NOE cross-peaks for base pairs C^2•G^{23}, T^3•A^{22}, A^4•T^{21}, G^5•C^{20}, C^6•G^{19}, X^7•C^{20}, A^8•T^{17}, G^9•C^{16}, T^{10}•A^{15}, and C^{11}•G^{14} were observed. X^7 N9H had NOE correlations with C^{18} N^4H(s) and A^8 H2 (Figure 3B). Notably, a strong X^7

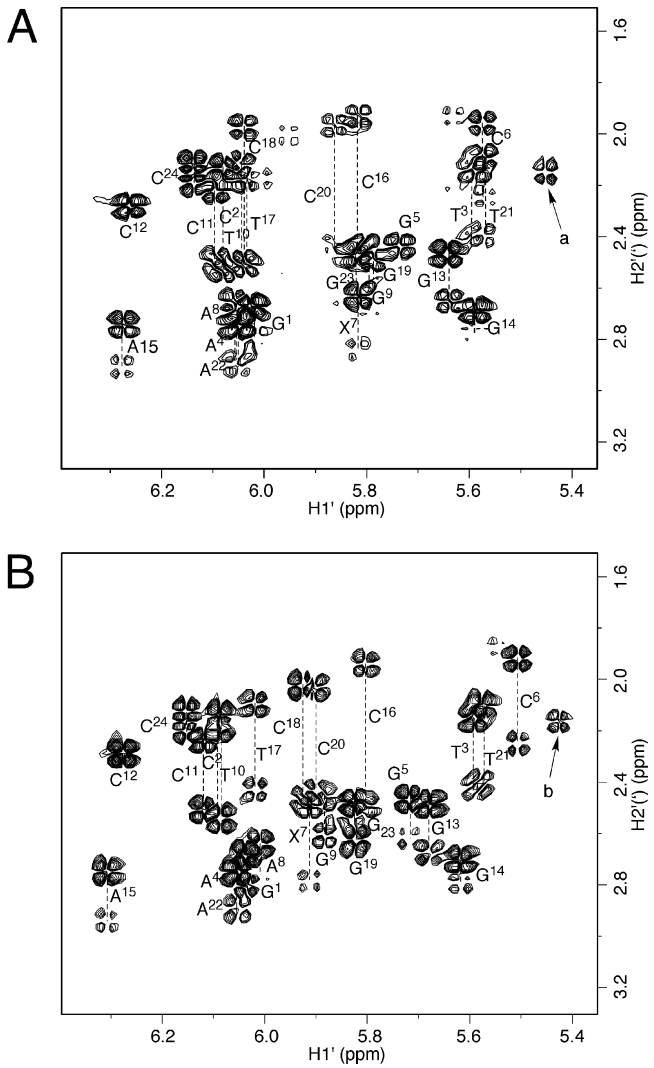

FIGURE 4: Expansions of DQF-COSY spectra of the oligodeoxynucleotide duplexes containing the 5′-CpX-3′ sequence, showing the H1′ → H2′(′) correlations. (A) Duplex containing cyclic hemiacetal **8**. (B) Duplex containing cyclic hemiacetal **10**. The peaks designated a and b were assigned to the X^7 H8 → X^7 H7 correlations.

N9H → X^7 N5H correlation was observed, similar to that of the duplex containing adduct **8**. NOE correlations of some HNE protons with X^7 N9H and X^7 N5H were observed (Figure 3B).

(c) HNE Protons. The HNE proton resonances were assigned on the basis of a combination of COSY, DQF-COSY, TOCSY, and NOESY (60 ms mixing time) spectra and rMD calculations. The resonances of two X^7 H7 protons were not split. The X^7 H8 → X^7 H7 correlation was observed in the H1′ → H2′(′) correlation region in the DQF-COSY spectrum (Figure 4B). The X^7 H6 → X^7 H7 correlation appeared at 4.55/2.17 ppm. These assignments were evidenced by the NOESY spectrum (60 ms mixing time), in which the X^7 H7 protons exhibited strong cross-peaks with both X^7 H6 and X^7 H8. X^7 H6 also correlated with X^7 H11 in both NOESY and COSY spectra, and the X^7 H11 → X^7 H12 correlations in the COSY and NOESY data were used to assign the X^7 H12 protons. The X^7 H16 protons were the most upfield and correlated strongly with X^7 H15 in both COSY and NOESY spectra. The resonances of X^7 H13 and X^7 H14 were assigned using the same iterative strategy that

Table 1: Chemical Shifts of HNE Protons of Stereoisomer **8** and Related NOE Cross-Peaks Used as rMD Distance Restraints

proton	δ (ppm)	NOEs[a]
H6	3.93	X^7 H11 (s), X^7 H12$^\alpha$ (m), X^7 H12$^\beta$ (m), X^7 H13 (w), A^8 H2 (w), A^8 H8 (w), A^8 H1′ (s)
H7$^\alpha$	2.13	X^7 H6 (s), X^7 H11 (m), X^7 H12$^\alpha$ (m), X^7 H12$^\beta$ (w), A^8 H2 (m), A^8 H4′ (w)
H7$^\beta$	2.15	X^7 H6 (s), X^7 H11 (m), X^7 H12$^\alpha$ (m), X^7 H12$^\beta$ (w), X^7 H13 (w), A^8 H2 (m), A^8 H4′ (w)
H8	5.45	H7$^\alpha$ (s), H7$^\beta$ (s), X^7 H6 (w), X^7 H11 (w), X^7 H12$^\alpha$ (m), X^7 H12$^\beta$ (w), X^7 H13 (w), X^7 H15 (w), C^{18} H1′ (w), C^{18} H2″ (w), G^{19} H1′ (w), G^{19} H4′ (m), G^{19} H5′ (m), G^{19} H5″ (w)
H11	4.26	X^7 H12$^\alpha$ (s), X^7 H12$^\beta$ (s), X^7 H13 (m), X^7 H14 (m), X^7 H15 (m), X^7 H16 (w)
H12$^\alpha$	1.33	X^7 H16 (m), X^7 H1′ (w), X^7 H5′ (w), A^8 H4′ (w), A^8 H5′ (m), G^{19} H1′ (w), C^{20} H1′ (m)
H12$^\beta$	1.41	X^7 H1′ (w), X^7 H5′ (w), A^8 H4′ (w), A^8 H5′ (w), G^{19} H1′ (w), C^{20} H1′ (w)
H13	1.27	X^7 H16 (m), X^7 H1′ (w), X^7 H5′ (w), A^8 H4′ (w), A^8 H5′ (w), C^{20} H1′ (w)
H14	1.15	X^7 H16 (m), X^7 H1′ (m), X^7 H4′ (m), X^7 H5′ (m), X^7 H5″ (w), A^8 H3′ (w), A^8 H4′ (w), A^8 H5′ (w), C^{20} H1′ (w)
H15	1.20	X^7 H16 (s), X^7 H1′ (s), X^7 H3′ (w), X^7 H4′ (m), X^7 H5′ (s), X^7 H5″ (m), A^8 H3′ (w), A^8 H4′ (m), A^8 H5′ (s), A^8 H5″ (m), C^{20} H1′ (m)
H16	0.82	X^7 H1′ (m), X^7 H3′ (w), X^7 H4′ (s), X^7 H5′ (m), X^7 H5″ (m), A^8 H3′ (w), A^8 H4′ (w), A^8 H5′ (m), A^8 H5″ (m), C^{20} H1′ (w)

[a] Letters in parentheses indicate peak intensity: s, strong; m, medium; w, weak.

was described for the assignment of the HNE protons in stereoisomer **8**. Unfortunately, for stereoisomer **10**, the chemical shifts of protons H12−H15 were less resolved than for stereoisomer **8**. Thus, it was not possible to unambiguously assign all NOEs arising from these protons. The chemical shifts of the HNE protons and the assigned NOEs from stereoisomer **10** are listed in Table 3.

(d) Chemical Shift Perturbations. The chemical shift comparisons of the nonexchangeable pyrimidine H6, purine H8, and 2-deoxyribose H1′ protons versus those of the corresponding unmodified duplex are presented in panels C and D of Figure 5. Large perturbations were observed at the adducted base pair X^7•C^{18}. As compared to the G^7 and C^{18} 2-deoxyribose H1′ protons in the unmodified duplex, the X^7 and C^{18} 2-deoxyribose H1′ resonances are shifted downfield 0.42 and 0.31 ppm, respectively. Few chemical shift perturbations were observed for the pyrimidine H6 and purine H8 protons.

(e) NMR-Derived Distances. A total of 73 NOE cross-peaks associated with the HNE-derived cyclic hemiacetal protons were converted to distance restraints (Table 3). Figure 6B shows some of these distance restraints. Notably, NOE correlations were observed between X^7 H12−H15 protons and A^8 H2, as well as A^8 H1′, G^9 H1′, and T^{17} H1′, in the 3′-direction. On the other hand, X^7 H7 exhibited a strong NOE with G^{19} H1′, in the 5′-direction. These NOEs suggested that the cyclic hemiacetal moiety was located in the minor groove, with the tetrahydrofuran oriented in the 5′-direction and the aliphatic chain oriented in the 3′-direction.

(f) 2-Deoxyribose and Backbone Angle Conformations. 2-Deoxyribose and backbone angle conformations were determined from DQF-COSY and ^{31}P−H3′ HMBC correlations. Evaluation of the DQF-COSY spectrum revealed that

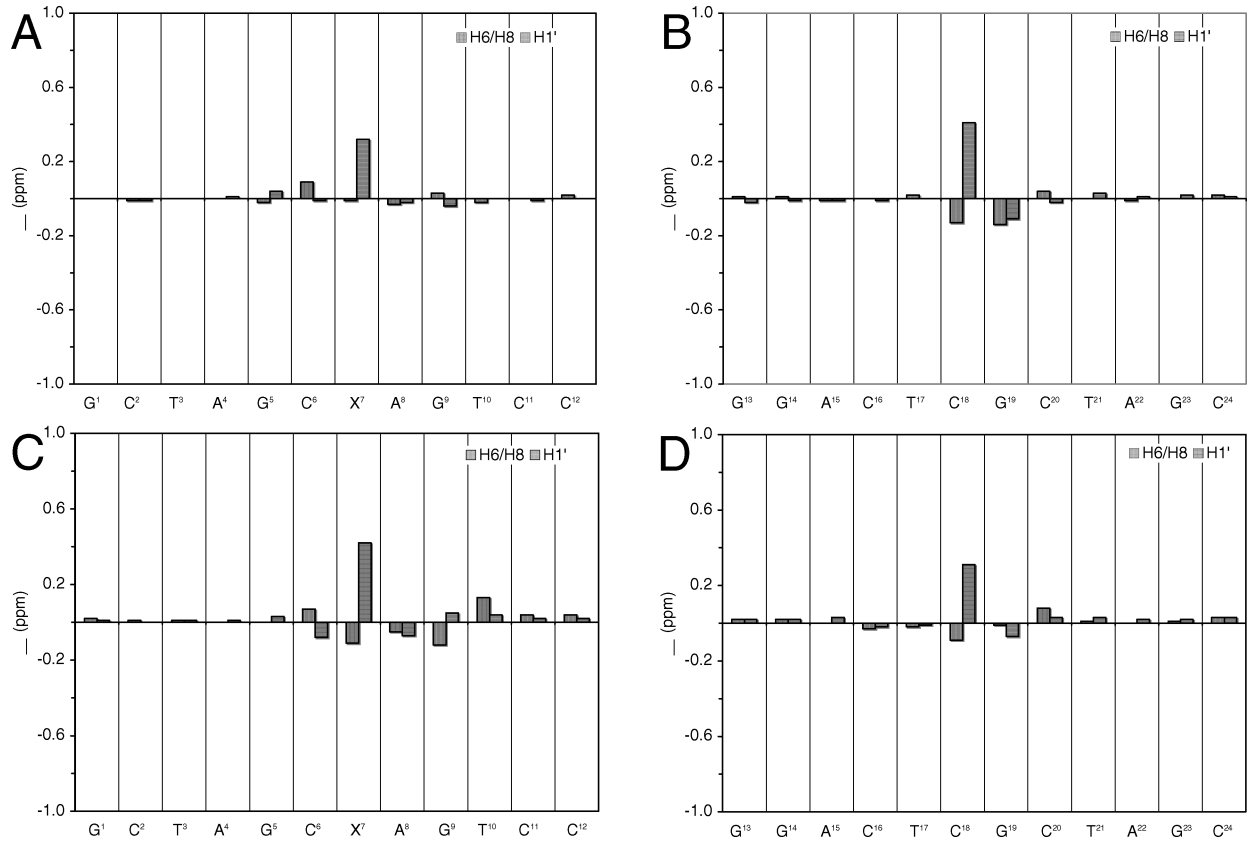

FIGURE 5: Proton chemical shift perturbations for the oligodeoxynucleotide duplexes containing the 5′-CpX-3′ sequence. (A) Modified strand of the duplex containing cyclic hemiacetal **8**. (B) Complementary strand of the duplex containing cyclic hemiacetal **8**. (C) Modified strand of the duplex containing cyclic hemiacetal **10**. (D) Complementary strand of the duplex containing cyclic hemiacetal **10**.

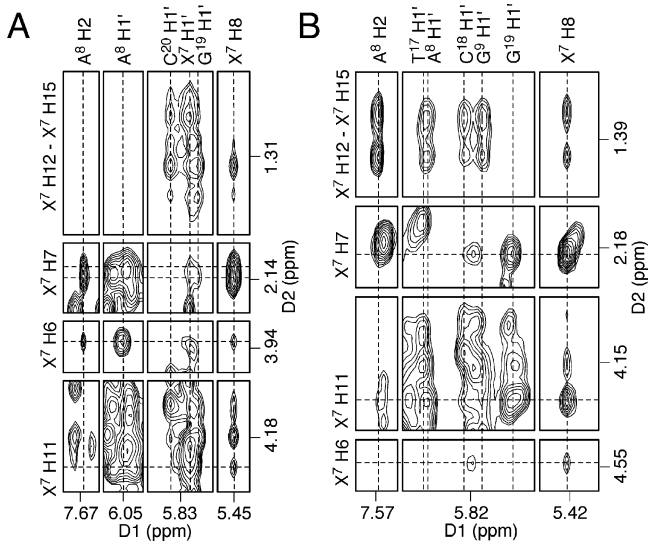

FIGURE 6: NOE correlations associated with the HNE protons, showing the different orientations of the HNE moieties in the oligodeoxynucleotide duplexes containing the 5′-CpX-3′ sequence. (A) Duplex containing cyclic hemiacetal **8**. (B) Duplex containing cyclic hemiacetal **10**.

the pseudorotations of the 2-deoxyribose rings for all residues were either $C_{1'}$-*exo* or $C_{2'}$-*endo*.

(g) Structure Refinement. The structural refinement employed 506 distance restraints, including 302 intraresidue and 204 interresidue restraints that were calculated from the intensities of the NOE cross-peaks. An additional 52 empirical distance restraints derived from Watson−Crick base pair interactions, as predicted by the NMR data, were used to refine the structure. Since the T^{17} N3H imino proton resonance was broad, a weak restraint was used for the $A^8 \cdot T^{17}$ Watson−Crick base pair. Finally, on the basis of analysis of the NMR data, 200 empirical backbone torsion angle restraints derived from B-DNA were also used (Table 4).

(h) rMD Computation. The randomly seeded rMD calculations were performed, starting from both initial A- and B-form geometries. Pairwise rmsd comparisons of the emergent structures indicated that the calculations converged, irrespective of starting structure (Table 4). The accuracies of the emergent structures were evaluated by comparison of

Table 2: rMD Restraints and Statistical Analysis of Structures Emergent from rMD Calculations Performed on the Oligodeoxynucleotide Duplex Site-Specifically Modified by Stereoisomer **8**

total no. of restraints for rMD calculation	780
no. of experimental NOE distance restraints[a]	528
no. of intraresidue NOE restraints	299
no. of interresidue NOE restraints	229
no. of restraints of the HNE unit	89
no. of empirical base pair restraints	52
no. of empirical torsion angle restraints	200
no. of backbone torsion angle restraints	100
no. of sugar torsion angle restraints	100
structure statistics	
NMR *R*-factor (R_1^x) ($\times 10^{-2}$)[b]	8.29
intraresidue NOEs	7.14
interresidue NOEs	10.0
rmsd of refined structures	0.42

[a] The HNE unit was considered to be a single residue attached to G^7 in the rMD calculations. [b] The mixing time used to calculate R_1^x was 250 ms. $R_1^x = \sum|(a_0)_i^{1/6} - (a_c)_i^{1/6}|/|(a_0)_i^{1/6}|$, where a_0 and a_c are the intensities of observed (non-zero) and calculated NOE cross-peaks, respectively.

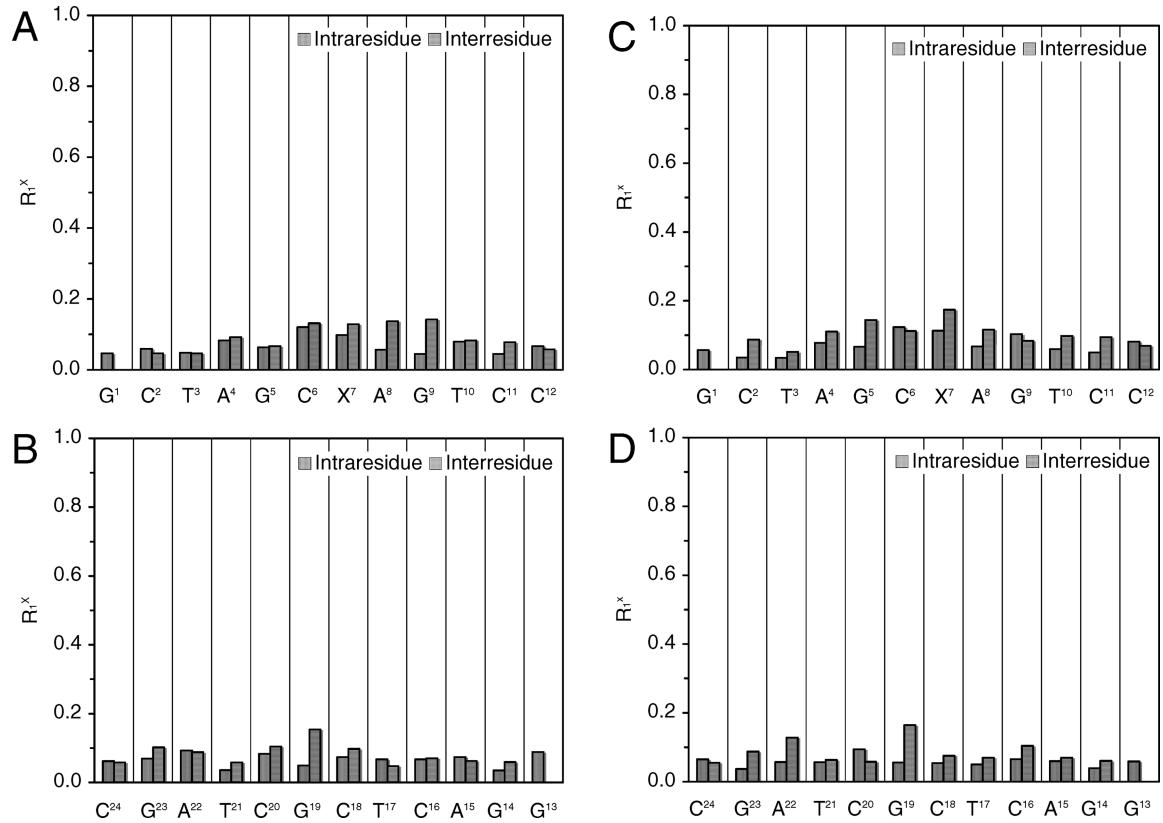

FIGURE 7: Residue-by-residue sixth-root residuals (R_1^x) of the oligodeoxynucleotide duplexes containing the 5′-CpX-3′ sequence, obtained from CORMA back calculation. (A) Modified strand of the duplex containing cyclic hemiacetal **8**. (B) Complementary strand of the duplex containing cyclic hemiacetal **8**. (C) Modified strand of the duplex containing cyclic hemiacetal **10**. (D) Complementary strand of the duplex containing cyclic hemiacetal **10**.

theoretical NOE intensities calculated by complete relaxation analysis to the experimental NOE intensities, to yield sixth-root residuals (R_1^x). The residual for the duplex was less than 0.1 (Table 4), and the inter- and intranucleotide residuals for each nucleotide were less than 0.15 (Figure 7C,D), indicating that the structures provided an accurate depiction of the data.

(i) Analysis of rMD Structures. The refined structures are overlaid in Figure 8B, and an expanded view of the adduct region of the average structure is shown in Figure 9C. The modified duplex remained in the B-type geometry. All nucleotides maintained the *anti* conformation about the glycosyl bond. Only minor torsion angle differences were observed as compared to canonical B-DNA. The 2-deoxyribose pseudorotations were consistently either $C_{1'}$-exo or $C_{2'}$-endo. The HNE-derived cyclic hemiacetal was folded in the minor groove of the duplex. In agreement with the NMR data, the tetrahydrofuran moiety was oriented in the 5′-direction and the aliphatic chain was oriented in the 3′-direction. Panels C and D of Figure 10 show the base stacking of the adduct region. The base stacking interactions were comparable to those observed for the unmodified duplex, although base pair $A^8 \cdot T^{17}$ exhibited an increased twist.

*Molecular Modeling of the Duplex Containing (6S,8R,11S) HNE-Derived Aldehydic Adduct **7**.* The refined structure of the cyclic hemiacetal **10** was then converted to the corresponding aldehyde **7**, which represented the reactive species necessary for DNA cross-link formation. At equilibrium, this species was not present in sufficient quantity to enable detailed structural refinement. Consequently, a molecular mechanics approach, using potential energy minimization, was employed to predict the conformation of aldehyde **7** in the minor groove of the DNA duplex. Figure 9D shows the predicted structure of the duplex containing aldehyde **7**. The HNE moiety remained in the minor groove. The aldehyde group was oriented in the 5′-direction.

DISCUSSION

Interest in the mechanism of HNE-mediated DNA interstrand cross-linking is based upon the observations that HNE is cytotoxic (*19–23*) and mutagenic (*29, 42–46*) and exocyclic 1,N^2-dG adducts **2**−**5** have been detected in cellular DNA (*30–36*). Moreover, as compared to the corresponding acrolein- and crotonaldehyde-induced exocyclic 1,N^2-dG adducts (*53, 57*), diastereomeric adduct **3** forms high levels of DNA interstrand cross-links at equilibrium, suggesting that the reversible cross-links associated with adduct **3**, once formed, are stable in duplex DNA (*51*).

*Conformations of the Duplexes Containing Stereoisomeric HNE-Derived Cyclic Hemiacetals **8** and **10**.* The stereoisomeric HNE-derived cyclic hemiacetals **8** and **10** were each accommodated within the minor groove of the DNA duplex (Figure 8). This conclusion emerged from consideration of a number of lines of evidence obtained from NMR data. Thus, the sequential NOE connectivity of both duplexes was complete for both the modified and complementary strands (Figure 1). In both instances, large chemical shift perturbations were observed only for the minor groove X^7 and C^{18} H1′ protons. The observation of NOE cross-peaks between HNE protons and A^8 H2 and A^8 H1′ minor groove protons

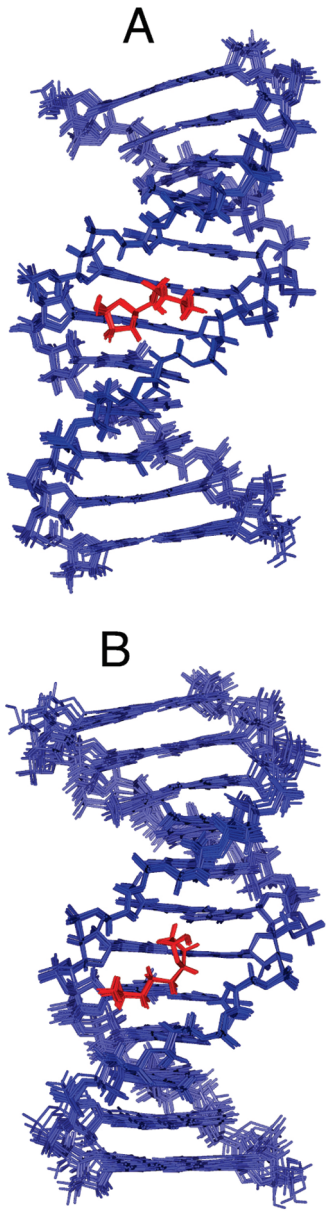

FIGURE 8: Refined structures obtained from rMD calculations for the oligodeoxynucleotide duplexes containing the 5′-CpX-3′ sequence. (A) Duplex containing cyclic hemiacetal **8**. (B) Duplex containing cyclic hemiacetal **10**. Blue sticks represent nucleotides and red sticks the HNE moiety.

indicated that the HNE-derived cyclic hemiacetals were positioned in the proximity of these protons (Tables 1 and 3). In contrast, there were no large chemical shift perturbations for the aromatic pyrimidine H6 or purine H8 protons, suggesting minimal changes to base stacking arrangements in the two modified duplexes (Figure 5). NOE correlations arising from Watson−Crick base pairs were observed for all nonterminal base pairs in both duplexes, also consistent with maintenance of Watson−Crick hydrogen bonding at the lesion sites (Figures 2 and 3). The exocyclic amine N5H protons of both stereoisomers **8** and **10** were observed as sharp resonances and showed strong NOEs to the imino N9H protons. At the adducted base pair, the base stacking of the duplex containing cyclic hemiacetal **8** was improved as compared to that of the duplex containing cyclic hemiacetal **10** (Figure 10). The A^8•T^{17} base pair in the duplex containing cyclic hemiacetal **10** adopted distorted Watson−Crick base pairing. This may partially explain the 4 °C reduction in melting temperature for this duplex (*51*). The NOESY spectrum of the duplex with stereoisomer **10** exhibited broadening of the T^{17} N3H imino proton (Figure 2B), and there were few NOEs assigned to this proton. This suggested that distortion of the A^8•T^{17} base pair resulted in a faster exchange of T^{17} N3H with solvent. On the other hand, the resonance of the T^{17} N3H imino proton in the duplex with cyclic hemiacetal **8** was sharp, and all anticipated NOEs arising from Watson−Crick base pairing were observed.

Role of Stereochemistry in DNA Interstrand Cross-Link Formation in the 5′-CpG-3′ Sequence. Among four stereoisomers of the exocyclic 1,N^2-dG HNE adduct, only adduct **3**, with (6*S*,8*R*,11*S*) stereochemistry, forms DNA interchain cross-linking in the 5′-CpG-3′ sequence (*51*). In duplex DNA, the cyclic hemiacetal stereoisomer **10** is the major species derived from exocyclic 1,N^2-dG stereoisomers **3** (*59*). Mechanistically, cross-linking requires adduct **7**, the aldehyde form of adduct **10**. Significantly, the orientations of the HNE-derived cyclic hemiacetals **8** and **10** differ (Figure 9). The NOE studies indicate that the tetrahydrofuran ring of stereoisomer **8** is directed toward the 3′-direction, while the tetrahydrofuran ring of stereoisomer **10** is directed toward the 5′-direction. The aliphatic chain of stereoisomer **8** exhibits NOEs with protons in the 5′-direction, and the tetrahydrofuran subunit correlates with protons in the 3′-direction (Figure 6). On the other hand, the aliphatic chain of stereoisomer **10** has NOEs with 3′-direction protons, and the tetrahydrofuran subunit has NOEs with 5′-direction protons (Figure 6). The presence of the long aliphatic chain within the minor groove suggests that the rotation of the HNE-derived cyclic hemiacetals around the X^7 N5−X^7 C6 bond is likely to be restrained. Consequently, to the extent that the cyclic hemiacetals open to unmask the corresponding aldehydes **6** and **7**, the latter are anticipated to adopt orientations similar to those of the respective cyclic hemiacetals **8** and **10**, from which they are derived. Therefore, the (6*S*,8*R*,11*S*) stereoisomer of the HNE-derived exocyclic 1,N^2-dG adduct **3**, which exists predominantly in duplex DNA as cyclic hemiacetal **10**, is positioned to facilitate interstrand cross-linking in the 5′-CpG-3′ sequence. In contrast, the (6*R*,8*S*,11*R*) stereoisomer of the HNE-derived exocyclic 1,N^2-dG adduct **2**, which exists in duplex DNA predominantly as cyclic hemiacetal **8**, is not positioned to facilitate interstrand cross-link formation. Molecular modeling of the respective aldehydes, **6** and **7**, is consistent with this conclusion (Figure 9B,D). Aldehyde **6**, which is in equilibrium with cyclic hemiacetals **8** and **9**, is predicted to be oriented in the 3′-direction, whereas aldehyde **7**, which is in equilibrium with cyclic hemiacetals **10** and **11**, is predicted to be oriented in the 5′-direction. Thus, aldehyde **7**, arising from exocyclic 1,N^2-dG adduct **3**, is predicted to be proximate to the C^6•G^{19} base pair, facilitating formation of the interstrand cross-link in the 5′-CpG-3′ sequence context.

Comparison to the (6R)- and (6S)-Crotonaldehyde-Derived Exocyclic 1,N^2-dG Adducts. Kozekov et al. (*53*) reported that the (6*R*) configuration of the crotonaldehyde-derived exocyclic 1,N^2-dG adduct produced a greater percentage of DNA interstrand cross-links than did the (6*S*) configuration. Significantly, at the C6 position, the relative stereochemistry of the (6*R*) crotonaldehyde-derived exocyclic 1,N^2-dG adduct

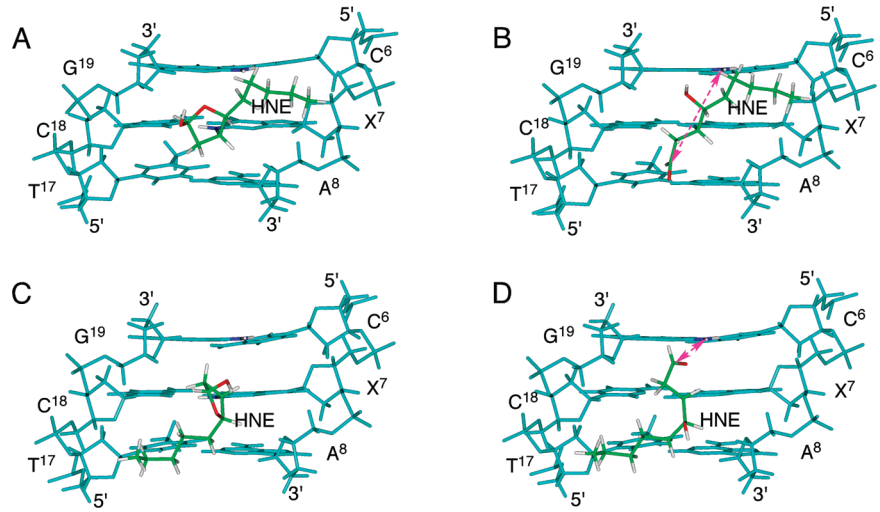

FIGURE 9: Adducted regions of the oligodeoxynucleotide duplexes containing the 5′-CpX-3′ sequence, viewed from the minor grooves. (A) Average refined structure emergent from rMD calculations of the duplex containing cyclic hemiacetal **8**. (B) Predicted structure, obtained by molecular mechanics calculations, of the duplex containing aldehyde **6**. The dashed arrows indicate the spatial relationship between the reactive aldehyde carbon and the exocyclic amino nitrogen of cross-linking target G^{19} (7.1 Å). (C) Average refined structure emergent from rMD calculations of the duplex containing cyclic hemiacetal **10**. (D) Predicted structure, obtained by molecular mechanics calculations, of the duplex containing aldehyde **7**. The cyan sticks represent nucleotides. The blue sticks represent the two amino nitrogens of X^7 and G^{19}. The white, green, and red sticks represent hydrogens, carbons, and oxygens of the HNE moiety, respectively. The dashed arrows indicate the spatial relationship between the reactive aldehyde carbon and the exocyclic amino nitrogen of cross-linking target G^{19} (4.4 Å).

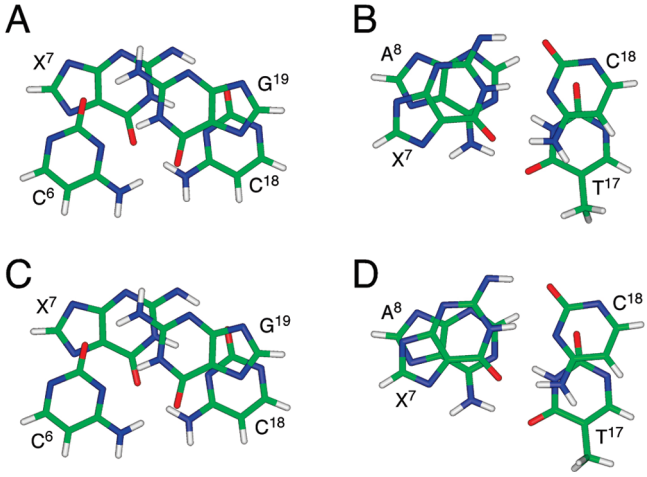

FIGURE 10: Base stacking of the adduct region for oligodeoxynucleotide duplexes containing the 5′-CpX-3′ sequence. (A) Duplex containing cyclic hemiacetal **8**. Stacking of base pair $C^6 \cdot G^{19}$ above base pair $X^7 \cdot C^{18}$. (B) Duplex containing cyclic hemiacetal **8**. Stacking of base pair $X^7 \cdot C^{18}$ above base pair $A^8 \cdot T^{17}$. (C) Duplex containing cyclic hemiacetal **10**. Stacking of base pair $C^6 \cdot G^{19}$ above base pair $X^7 \cdot C^{18}$. (D) Duplex containing cyclic hemiacetal **10**. Stacking of base pair $X^7 \cdot C^{18}$ above base pair $A^8 \cdot T^{17}$. For both duplexes containing either cyclic hemiacetal **8** or **10**, base pairs $C^6 \cdot G^{19}$, $X^7 \cdot C^{18}$, and $A^8 \cdot T^{17}$ adopt Watson−Crick pairing.

Table 3: Chemical Shifts of HNE Protons of Stereoisomer **10** and Related NOE Cross-Peaks Used as rMD Distance Restraints

proton	δ (ppm)	NOEs[a]
H6	4.55	X^7 H11 (s), X^7 H12$^\alpha$ (w), X^7 H12$^\beta$ (m), X^7 6A (w), X^7 H1′ (w), A^8 H1′ (w), G^{19} H1′ (w)
H7	2.17	X^7 H6 (s), X^7 H11 (m), X^7 H12$^\alpha$ (s), X^7 H12$^\beta$ (s), X^7 H13 (s), X^7 H1′ (w), C^{18} H1′ (w), G^{19} H1′ (s)
H8	5.43	X^7 H7 (s), X^7 H6 (m), X^7 H11 (m), X^7 H12$^\alpha$ (w), X^7 H12$^\beta$ (m), X^7 H13 (m), C^{18} H1′ (w), G^{19} H1′ (w), G^{19} H4′ (m), G^{19} H5′ (w), G^{19} H5″ (w), C^{20} H5′ (w)
H11	4.23	X^7 H12$^\alpha$ (s), X^7 H12$^\beta$ (s), X^7 H13 (s), A^8 H2 (s)
H12$^\alpha$	1.34	A^8 H2 (m), A^8 H1′ (m), A^8 H4′ (m), G^9 H2′ (w), G^9 H2″ (w)
H12$^\beta$	1.45	A^8 H2 (m), A^8 H1′ (m), A^8 H4′ (m)
H13	1.36	X^7 H16 (s), A^8 H2 (m), A^8 H1′ (m), A^8 H4′ (m), G^9 H1′ (m), G^9 H4′ (m), T^{17} H1′ (m), C^{18} H1′ (m)
H14	1.45	X^7 H16 (m), A^8 H2 (m), A^8 H4′ (m), G^9 H1′ (m), G^9 H2′ (w), G^9 H2″ (w), G^9 H4′ (m), T^{17} H1′ (w), C^{18} H1′ (m)
H15	1.38	X^7 H16 (s), A^8 H2 (w), G^9 H1′ (m), G^9 H4′ (m), G^9 H2″ (w), T^{17} H1′ (w), C^{18} H1′ (w)
H16	0.96	G^9 H1′ (w), G^9 H5′ (w), G^9 H4′ (w), G^9 H5″ (w), T^{10} H5′ (w), T^{10} H5″ (w), C^{18} H1′ (w), C^{18} H4′ (m), C^{18} H5′ (w), C^{18} H5″ (w)

[a] Letters in parentheses indicate peak intensity: s, strong; m, medium; w, weak.

corresponds to the (6*S*,8*R*,11*S*) stereochemistry of the HNE-derived exocyclic 1,N^2-dG adduct **3**. Thus, we conclude that the cyclic hemiacetal arising in duplex DNA from HNE-derived adduct **3** facilitates interstrand cross-linking for the same reason that the (6*R*)-crotonaldehyde-derived adduct does (*56*); it places the requisite aldehyde in the minor groove proximal to the cross-linking target in the 5′-CpG-3′ sequence context. In contrast, cyclic hemiacetal **8**, arising from the (6*R*,8*S*,11*R*) stereochemistry of the HNE-derived exocyclic 1,N^2-dG adduct **2**, places the requisite aldehydic species in the minor groove distal to the cross-linking target in the 5′-CpG-3′ sequence context. Again, this is similar to what was observed for the (6*S*)-crotonaldehyde-derived adduct, in which the aldehyde oriented toward the $A^8 \cdot T^{17}$ base pair, distal to the targeted C·G base pair (*90*). In contrast to HNE, the crotonaldehyde alkyl chain is small with regard to the width of the minor groove, which allows the aldehydic form of the (6*S*)-crotonaldehyde adduct to transiently undergo conformational reorientation in which the aldehyde orients toward the cross-linking target $C^6 \cdot G^{19}$ base pair. This probably explains why a small amount of cross-link was observed (<5% cross-link) for the (6*S*)-crotonaldehyde-derived adduct (*53*). However, the reduced form of the (6*S*)-crotonaldehyde-derived cross-link was less stable than the favored (6*R*)-crotonaldehyde-derived cross-link (*91*), consistent with modeling studies (*56*). Provided the interchain cross-link was induced by cyclic hemiacetal **8**, we anticipate that the long HNE aliphatic chain should induce a greater

Table 4: rMD Restraints and Statistical Analysis of Structures Emergent from rMD Calculations Performed on the Oligodeoxynucleotide Duplex Site-Specifically Modified by Stereoisomer **10**

total no. of restraints for rMD calculation	760
no. of experimental NOE distance restraints[a]	508
no. of intraresidue NOE restraints	302
no. of interresidue NOE restraints	206
no. of restraints of the HNE unit	73
no. of empirical base pair restraints	52
no. of empirical torsion angle restraints	200
no. of backbone torsion angle restraints	100
no. of sugar torsion angle restraints	100
structure statistics	
NMR *R*-factor (R_1^x) ($\times 10^{-2}$)[b]	7.87
intraresidue NOEs	6.75
interresidue NOEs	9.74
rmsd of refined structures	0.53

[a] The HNE unit was considered to be an single residue attached to G^7 in the rMD calculations. [b] The mixing time used to calculate R_1^x was 250 ms. $R_1^x = \sum|(a_0)_i^{1/6} - (a_c)_i^{1/6}|/|(a_0)_i^{1/6}|$, where a_0 and a_c are the intensities of observed (non-zero) and calculated NOE cross-peaks, respectively.

destabilization of the DNA duplex, as compared to the (6*S*)-crotonaldehyde-derived adduct. Consequently, structural analysis of the cross-linked species arising from the (6*R*,8*S*,11*R*) and (6*S*,8*R*,11*S*) HNE-derived adducts **2** and **3** will be of considerable interest.

Biological Implications. In light of the observation that the (6*S*,8*R*,11*S*) HNE-derived adduct **3** forms DNA interstrand cross-links in 5′-CpG-3′ DNA sequences in vitro (*51*), we anticipate that it will also form interstrand cross-links in vivo. It will now be of considerable interest to search for this reversible HNE-derived interstrand cross-link in cellular DNA. It occurs specifically at 5′-CpG-3′ sequences, and only for HNE-derived diastereomeric adduct **3**, and is consequently expected to be present at low levels in vivo, challenging the limits of detection by mass spectrometry (*92–96*). On the other hand, the potential biological consequences arising from low levels of this interstrand DNA cross-link may be of considerable genotoxic significance.

CONCLUSIONS

The solution structures of the stereoisomeric cyclic hemiacetals arising from the (6*R*,8*S*,11*R*) and (6*S*,8*R*,11*S*) HNE-derived exocyclic 1,N^2-dG adducts **2** and **3** were obtained in a DNA duplex containing the 5′-CpG-3′ sequence motif in which adduct **3**, but not adduct **2**, forms interstrand cross-links. The orientations of the cyclic hemiacetal groups within the minor groove differ for the two diastereoisomers. The tetrahydrofuran ring of cyclic hemiacetal **10**, arising from adduct **3** with (6*S*,8*R*,11*S*) stereochemistry, masking the aldehydic species necessary for cross-link formation, is oriented in the 5′-direction toward base pair $C^6 \cdot G^{19}$, while the tetrahydrofuran ring of cyclic hemiacetal **8**, arising from adduct **2** with (6*R*,8*S*,11*R*) stereochemistry, masking the aldehydic species necessary for cross-link formation, is oriented in the 3′-direction toward base pair $A^8 \cdot T^{17}$. Thus, HNE-derived adduct **3** with (6*S*,8*R*,11*S*) stereochemistry facilitates formation of interstrand cross-links, whereas HNE-derived adduct **2** with (6*R*,8*S*,11*R*) stereochemistry does not form interstrand cross-links in DNA.

ACKNOWLEDGMENT

Dr. Markus Voehler assisted with NMR experiments, and Ms. Albena Kozekova assisted with oligodeoxynucleotide synthesis.

SUPPORTING INFORMATION AVAILABLE

^{1}H chemical shift assignments of the 5′-CpG-3′ duplex with stereoisomer **8** (Table S1), ^{1}H chemical shift assignments of the 5′-CpG-3′ duplex with stereoisomer **10** (Table S2), NOE restraints utilized in the rMD calculation for the 5′-CpG-3′ duplex with stereoisomer **8** (Table S3), NOE restraints utilized in the rMD calculation for the 5′-CpG-3′ duplex with stereoisomer **10** (Table S4), backbone torsion angles derived from rMD structure of stereoisomer **8** (Table S5), backbone torsion angles derived from the rMD structure of stereoisomer **10** (Table S6), and force field parameters of stereoisomers **8** and **10** used for rMD calculation (Figure S1). This material is available free of charge via the Internet at http://pubs.acs.org.

REFERENCES

1. Benedetti, A., Comporti, M., and Esterbauer, H. (1980) Identification of 4-hydroxynonenal as a cytotoxic product originating from the peroxidation of liver microsomal lipids. *Biochim. Biophys. Acta 620*, 281–296.
2. Esterbauer, H., Schaur, R. J., and Zollner, H. (1991) Chemistry and biochemistry of 4-hydroxynonenal, malonaldehyde and related aldehydes. *Free Radical Biol. Med. 11*, 81–128.
3. Burcham, P. C. (1998) Genotoxic lipid peroxidation products: Their DNA damaging properties and role in formation of endogenous DNA adducts. *Mutagenesis 13*, 287–305.
4. Lee, S. H., and Blair, I. A. (2000) Characterization of 4-oxo-2-nonenal as a novel product of lipid peroxidation. *Chem. Res. Toxicol. 13*, 698–702.
5. Schneider, C., Tallman, K. A., Porter, N. A., and Brash, A. R. (2001) Two distinct pathways of formation of 4-hydroxynonenal. Mechanisms of nonenzymatic transformation of the 9- and 13-hydroperoxides of linoleic acid to 4-hydroxyalkenals. *J. Biol. Chem. 276*, 20831–20838.
6. Schneider, C., Porter, N. A., and Brash, A. R. (2008) Routes to 4-hydroxynonenal: Fundamental issues in the mechanisms of lipid peroxidation. *J. Biol. Chem. 283*, 15539–15543.
7. Parola, M., Bellomo, G., Robino, G., Barrera, G., and Dianzani, M. U. (1999) 4-Hydroxynonenal as a biological signal: Molecular basis and pathophysiological implications. *Antioxid. Redox Signal. 1*, 255–284.
8. Poli, G., and Schaur, R. J. (2000) 4-Hydroxynonenal in the pathomechanisms of oxidative stress. *IUBMB Life 50*, 315–321.
9. Nakashima, I., Liu, W., Akhand, A. A., Takeda, K., Kawamoto, Y., Kato, M., and Suzuki, H. (2003) 4-Hydroxynonenal triggers multistep signal transduction cascades for suppression of cellular functions. *Mol. Aspects Med. 24*, 231–238.
10. West, J. D., Ji, C., Duncan, S. T., Amarnath, V., Schneider, C., Rizzo, C. J., Brash, A. R., and Marnett, L. J. (2004) Induction of apoptosis in colorectal carcinoma cells treated with 4-hydroxy-2-nonenal and structurally related aldehydic products of lipid peroxidation. *Chem. Res. Toxicol. 17*, 453–462.
11. West, J. D., and Marnett, L. J. (2005) Alterations in gene expression induced by the lipid peroxidation product, 4-hydroxy-2-nonenal. *Chem. Res. Toxicol. 18*, 1642–1653.
12. West, J. D., and Marnett, L. J. (2006) Endogenous reactive intermediates as modulators of cell signaling and cell death. *Chem. Res. Toxicol. 19*, 173–194.
13. Dwivedi, S., Sharma, A., Patrick, B., Sharma, R., and Awasthi, Y. C. (2007) Role of 4-hydroxynonenal and its metabolites in signaling. *Redox Rep. 12*, 4–10.
14. Sayre, L. M., Zelasko, D. A., Harris, P. L., Perry, G., Salomon, R. G., and Smith, M. A. (1997) 4-Hydroxynonenal-derived advanced lipid peroxidation end products are increased in Alzheimer's disease. *J. Neurochem. 68*, 2092–2097.

15. Yoritaka, A., Hattori, N., Uchida, K., Tanaka, M., Stadtman, E. R., and Mizuno, Y. (1996) Immunohistochemical detection of 4-hydroxynonenal protein adducts in Parkinson disease. *Proc. Natl. Acad. Sci. U.S.A. 93*, 2696–2701.
16. Napoli, C., D'Armiento, F. P., Mancini, F. P., Postiglione, A., Witztum, J. L., Palumbo, G., and Palinski, W. (1997) Fatty streak formation occurs in human fetal aortas and is greatly enhanced by maternal hypercholesterolemia. Intimal accumulation of low density lipoprotein and its oxidation precede monocyte recruitment into early atherosclerotic lesions. *J. Clin. Invest. 100*, 2680–2690.
17. Yamagami, K., Yamamoto, Y., Kume, M., Ishikawa, Y., Yamaoka, Y., Hiai, H., and Toyokuni, S. (2000) Formation of 8-hydroxy-2′-deoxyguanosine and 4-hydroxy-2-nonenal-modified proteins in rat liver after ischemia-reperfusion: Distinct localization of the two oxidatively modified products. *Antioxid. Redox Signal. 2*, 127–136.
18. Benamira, M., and Marnett, L. J. (1992) The lipid peroxidation product 4-hydroxynonenal is a potent inducer of the SOS response. *Mutat. Res. 293*, 1–10.
19. Esterbauer, H., Eckl, P., and Ortner, A. (1990) Possible mutagens derived from lipids and lipid precursors. *Mutat. Res. 238*, 223–233.
20. Eckl, P. M., Ortner, A., and Esterbauer, H. (1993) Genotoxic properties of 4-hydroxyalkenals and analogous aldehydes. *Mutat. Res. 290*, 183–192.
21. Karlhuber, G. M., Bauer, H. C., and Eckl, P. M. (1997) Cytotoxic and genotoxic effects of 4-hydroxynonenal in cerebral endothelial cells. *Mutat. Res. 381*, 209–216.
22. Eckl, P. M. (2003) Genotoxicity of HNE. *Mol. Aspects Med. 24*, 161–165.
23. Emerit, I., Khan, S. H., and Esterbauer, H. (1991) Hydroxynonenal, a component of clastogenic factors? *Free Radical Biol. Med. 10*, 371–377.
24. Chung, F. L., Komninou, D., Zhang, L., Nath, R., Pan, J., Amin, S., and Richie, J. (2005) Glutathione depletion enhances the formation of endogenous cyclic DNA adducts derived from *t*-4-hydroxy-2-nonenal in rat liver. *Chem. Res. Toxicol. 18*, 24–27.
25. Falletti, O., Cadet, J., Favier, A., and Douki, T. (2007) Trapping of 4-hydroxynonenal by glutathione efficiently prevents formation of DNA adducts in human cells. *Free Radical Biol. Med. 42*, 1258–1269.
26. Yadav, U. C., Ramana, K. V., Awasthi, Y. C., and Srivastava, S. K. (2008) Glutathione level regulates HNE-induced genotoxicity in human erythroleukemia cells. *Toxicol. Appl. Pharmacol. 227*, 257–264.
27. Winter, C. K., Segall, H. J., and Haddon, W. F. (1986) Formation of cyclic adducts of deoxyguanosine with the aldehydes *trans*-4-hydroxy-2-hexenal and *trans*-4-hydroxy-2-nonenal *in vitro*. *Cancer Res. 46*, 5682–5686.
28. Douki, T., Odin, F., Caillat, S., Favier, A., and Cadet, J. (2004) Predominance of the 1,N^2-propano 2′-deoxyguanosine adduct among 4-hydroxy-2-nonenal-induced DNA lesions. *Free Radical Biol. Med. 37*, 62–70.
29. Kowalczyk, P., Ciesla, J. M., Komisarski, M., Kusmierek, J. T., and Tudek, B. (2004) Long-chain adducts of *trans*-4-hydroxy-2-nonenal to DNA bases cause recombination, base substitutions and frameshift mutations in M13 phage. *Mutat. Res. 550*, 33–48.
30. Yi, P., Zhan, D., Samokyszyn, V. M., Doerge, D. R., and Fu, P. P. (1997) Synthesis and ^{32}P-postlabeling/high-performance liquid chromatography separation of diastereomeric 1,N^2-(1,3-propano)-2′-deoxyguanosine 3′-phosphate adducts formed from 4-hydroxy-2-nonenal. *Chem. Res. Toxicol. 10*, 1259–1265.
31. Chung, F. L., Nath, R. G., Ocando, J., Nishikawa, A., and Zhang, L. (2000) Deoxyguanosine adducts of *t*-4-hydroxy-2-nonenal are endogenous DNA lesions in rodents and humans: Detection and potential sources. *Cancer Res. 60*, 1507–1511.
32. Wacker, M., Schuler, D., Wanek, P., and Eder, E. (2000) Development of a ^{32}P-postlabeling method for the detection of 1,N^2-propanodeoxyguanosine adducts of *trans*-4-hydroxy-2-nonenal *in vivo*. *Chem. Res. Toxicol. 13*, 1165–1173.
33. Wacker, M., Wanek, P., and Eder, E. (2001) Detection of 1,N^2-propanodeoxyguanosine adducts of *trans*-4-hydroxy-2-nonenal after gavage of *trans*-4-hydroxy-2-nonenal or induction of lipid peroxidation with carbon tetrachloride in F344 rats. *Chem.-Biol. Interact. 137*, 269–283.
34. Chung, F. L., and Zhang, L. (2002) Deoxyguanosine adducts of *tert*-4-hydroxy-2-nonenal as markers of endogenous DNA lesions. *Methods Enzymol. 353*, 523–536.
35. Liu, X., Lovell, M. A., and Lynn, B. C. (2006) Detection and quantification of endogenous cyclic DNA adducts derived from *trans*-4-hydroxy-2-nonenal in human brain tissue by isotope dilution capillary liquid chromatography nanoelectrospray tandem mass spectrometry. *Chem. Res. Toxicol. 19*, 710–718.
36. Pan, J., Davis, W., Trushin, N., Amin, S., Nath, R. G., Salem, N., Jr., and Chung, F. L. (2006) A solid-phase extraction/high-performance liquid chromatography-based ^{32}P-postlabeling method for detection of cyclic 1,N^2-propanodeoxyguanosine adducts derived from enals. *Anal. Biochem. 348*, 15–23.
37. Sodum, R. S., and Chung, F. L. (1988) 1,N^2-Ethenodeoxyguanosine as a potential marker for DNA adduct formation by *trans*-4-hydroxy-2-nonenal. *Cancer Res. 48*, 320–323.
38. Sodum, R. S., and Chung, F. L. (1989) Structural characterization of adducts formed in the reaction of 2,3-epoxy-4-hydroxynonanal with deoxyguanosine. *Chem. Res. Toxicol. 2*, 23–28.
39. Sodum, R. S., and Chung, F. L. (1991) Stereoselective formation of *in vitro* nucleic acid adducts by 2,3-epoxy-4-hydroxynonanal. *Cancer Res. 51*, 137–143.
40. Chen, H. J., and Chung, F. L. (1994) Formation of etheno adducts in reactions of enals via autoxidation. *Chem. Res. Toxicol. 7*, 857–860.
41. el Ghissassi, F., Barbin, A., Nair, J., and Bartsch, H. (1995) Formation of 1,N^6-ethenoadenine and 3,N^4-ethenocytosine by lipid peroxidation products and nucleic acid bases. *Chem. Res. Toxicol. 8*, 278–283.
42. Cajelli, E., Ferraris, A., and Brambilla, G. (1987) Mutagenicity of 4-hydroxynonenal in V79 Chinese hamster cells. *Mutat. Res. 190*, 169–171.
43. Chung, F. L., Chen, H. J., Guttenplan, J. B., Nishikawa, A., and Hard, G. C. (1993) 2,3-Epoxy-4-hydroxynonanal as a potential tumor-initiating agent of lipid peroxidation. *Carcinogenesis 14*, 2073–2077.
44. Hussain, S. P., Raja, K., Amstad, P. A., Sawyer, M., Trudel, L. J., Wogan, G. N., Hofseth, L. J., Shields, P. G., Billiar, T. R., Trautwein, C., Hohler, T., Galle, P. R., Phillips, D. H., Markin, R., Marrogi, A. J., and Harris, C. C. (2000) Increased p53 mutation load in nontumorous human liver of Wilson disease and hemochromatosis: Oxyradical overload diseases. *Proc. Natl. Acad. Sci. U.S.A. 97*, 12770–12775.
45. Hu, W., Feng, Z., Eveleigh, J., Iyer, G., Pan, J., Amin, S., Chung, F. L., and Tang, M. S. (2002) The major lipid peroxidation product, trans-4-hydroxy-2-nonenal, preferentially forms DNA adducts at codon 249 of human p53 gene, a unique mutational hotspot in hepatocellular carcinoma. *Carcinogenesis 23*, 1781–1789.
46. Feng, Z., Hu, W., Amin, S., and Tang, M. S. (2003) Mutational spectrum and genotoxicity of the major lipid peroxidation product trans-4-hydroxy-2-nonenal, induced DNA adducts in nucleotide excision repair-proficient and -deficient human cells. *Biochemistry 42*, 7848–7854.
47. Fernandes, P. H., Wang, H., Rizzo, C. J., and Lloyd, R. S. (2003) Site-specific mutagenicity of stereochemically defined 1,N^2-deoxyguanosine adducts of *trans*-4-hydroxynonenal in mammalian cells. *Environ. Mol. Mutagen. 42*, 68–74.
48. Chung, F. L., Pan, J., Choudhury, S., Roy, R., Hu, W., and Tang, M. S. (2003) Formation of *trans*-4-hydroxy-2-nonenal- and other enal-derived cyclic DNA adducts from ω-3 and ω-6 polyunsaturated fatty acids and their roles in DNA repair and human p53 gene mutation. *Mutat. Res. 531*, 25–36.
49. Choudhury, S., Pan, J., Amin, S., Chung, F. L., and Roy, R. (2004) Repair kinetics of *trans*-4-hydroxynonenal-induced cyclic 1,N^2-propanodeoxyguanine DNA adducts by human cell nuclear extracts. *Biochemistry 43*, 7514–7521.
50. Wang, H., and Rizzo, C. J. (2001) Stereocontrolled syntheses of all four stereoisomeric 1,N^2-deoxyguanosine adducts of the lipid peroxidation product *trans*-4-hydroxynonenal. *Org. Lett. 3*, 3603–3605.
51. Wang, H., Kozekov, I. D., Harris, T. M., and Rizzo, C. J. (2003) Site-specific synthesis and reactivity of oligonucleotides containing stereochemically defined 1,N^2-deoxyguanosine adducts of the lipid peroxidation product *trans*-4-hydroxynonenal. *J. Am. Chem. Soc. 125*, 5687–5700.
52. Kozekov, I. D., Nechev, L. V., Sanchez, A., Harris, C. M., Lloyd, R. S., and Harris, T. M. (2001) Interchain cross-linking of DNA mediated by the principal adduct of acrolein. *Chem. Res. Toxicol. 14*, 1482–1485.
53. Kozekov, I. D., Nechev, L. V., Moseley, M. S., Harris, C. M., Rizzo, C. J., Stone, M. P., and Harris, T. M. (2003) DNA interchain

cross-links formed by acrolein and crotonaldehyde. *J. Am. Chem. Soc. 125*, 50–61.
54. Kim, H. Y., Voehler, M., Harris, T. M., and Stone, M. P. (2002) Detection of an interchain carbinolamine cross-link formed in a CpG sequence by the acrolein DNA adduct γ-OH-1,N^2-propano-2′-deoxyguanosine. *J. Am. Chem. Soc. 124*, 9324–9325.
55. Cho, Y. J., Kim, H. Y., Huang, H., Slutsky, A., Minko, I. G., Wang, H., Nechev, L. V., Kozekov, I. D., Kozekova, A., Tamura, P., Jacob, J., Voehler, M., Harris, T. M., Lloyd, R. S., Rizzo, C. J., and Stone, M. P. (2005) Spectroscopic characterization of interstrand carbinolamine cross-links formed in the 5′-CpG-3′ sequence by the acrolein-derived γ-OH-1,N^2-propano-2′-deoxyguanosine DNA adduct. *J. Am. Chem. Soc. 127*, 17686–17696.
56. Cho, Y. J., Wang, H., Kozekov, I. D., Kurtz, A. J., Jacob, J., Voehler, M., Smith, J., Harris, T. M., Lloyd, R. S., Rizzo, C. J., and Stone, M. P. (2006) Stereospecific formation of interstrand carbinolamine DNA cross-links by crotonaldehyde- and acetaldehyde-derived α-CH_3-γ-OH-1,N^2-propano-2′-deoxyguanosine adducts in the 5′-CpG-3′ sequence. *Chem. Res. Toxicol. 19*, 195–208.
57. Stone, M. P., Cho, Y.-J., Huang, H., Kim, H.-Y., Kozekov, I. D., Kozekova, A., Wang, H., Lloyd, R. S., Harris, T. M., and Rizzo, C. J. (2008) Interstrand DNA cross-links induced by α,β-unsaturated aldehydes derived from lipid peroxidation and environmental sources. *Acc. Chem. Res. 41*, 793–804.
58. Noll, D. M., Mason, T. M., and Miller, P. S. (2006) Formation and repair of interstrand cross-links in DNA. *Chem. Rev. 106*, 277–301.
59. Huang, H., Wang, H., Qi, N., Kozekova, A., Rizzo, C. J., and Stone, M. P. (2008) Rearrangement of the (6*S*,8*R*,11*S*) and (6*R*,8*S*,11*R*) exocyclic 1,N^2-deoxyguanosine adducts of *trans*-4-hydroxynonenal to N^2-deoxyguanosine cyclic hemiacetal adducts when placed complementary to cytosine in duplex DNA. *J. Am. Chem. Soc. 130*, 10898–10906.
60. Sayre, L. M., Lin, D., Yuan, Q., Zhu, X., and Tang, X. (2006) Protein adducts generated from products of lipid oxidation: Focus on HNE and ONE. *Drug Metab. Rev. 38*, 651–675.
61. Kurtz, A. J., and Lloyd, R. S. (2003) 1,N^2-Deoxyguanosine adducts of acrolein, crotonaldehyde, and *trans*-4-hydroxynonenal cross-link to peptides via Schiff base linkage. *J. Biol. Chem. 278*, 5970–5976.
62. Cavaluzzi, M. J., and Borer, P. N. (2004) Revised UV extinction coefficients for nucleoside-5′-monophosphates and unpaired DNA and RNA. *Nucleic Acids Res. 32*, e13.
63. Piotto, M., Saudek, V., and Sklenar, V. (1992) Gradient-tailored excitation for single-quantum NMR spectroscopy of aqueous solutions. *J. Biomol. NMR 2*, 661–665.
64. Sklenar, V., Bax, A., and Zon, G. (1986) Assignment of Z DNA NMR spectra of poly d($G^{m5}C$) by two-dimensional multinuclear spectroscopy. *FEBS Lett. 208*, 94–98.
65. Sklenar, V., Miyashiro, H., Zon, G., Miles, H. T., and Bax, A. (1986) Assignment of the ^{31}P and ^{1}H resonances in oligonucleotides by two-dimensional NMR spectroscopy. *FEBS Lett. 208*, 94–98.
66. James, T. L. (1991) Relaxation matrix analysis of two-dimensional nuclear Overhauser effect spectra. *Curr. Opin. Struct. Biol. 1*, 1042–1053.
67. Keepers, J. W., and James, T. L. (1984) A theoretical study of distance determinations from NMR: Two-dimensional nuclear Overhauser effect spectra. *J. Magn. Reson. 57*, 404–426.
68. Borgias, B. A., and James, T. L. (1989) Two-dimensional nuclear Overhauser effect: Complete relaxation matrix analysis. *Methods Enzymol. 176*, 169–183.
69. Borgias, B. A., and James, T. L. (1990) MARDIGRAS: A procedure for matrix analysis of relaxation for discerning geometry of an aqueous structure. *J. Magn. Reson. 87*, 475–487.
70. Liu, H., Spielmann, H. P., Ulyanov, N. B., Wemmer, D. E., and James, T. L. (1995) Interproton distance bounds from 2D NOE intensities: Effect of experimental noise and peak integration errors. *J. Biomol. NMR 6*, 390–402.
71. Salazar, M., Fedoroff, O. Y., Miller, J. M., Ribeiro, N. S., and Reid, B. R. (1993) The DNA strand in DNA:RNA hybrid duplexes is neither B-form nor A-form in solution. *Biochemistry 32*, 4207–4215.
72. Wang, H., Zuiderweg, E. R. P., and Glick, G. D. (1995) Solution structure of a disulfide cross-linked DNA hairpin. *J. Am. Chem. Soc. 117*, 2981–2991.
73. Geen, H., and Freeman, R. (1991) Band-selective radiofrequency pulses. *J. Magn. Reson. 93*, 93–141.
74. Lankhorst, P. P., Haasnoot, A. G., Erkelens, C., and Altona, C. (1984) Carbon-13 NMR in conformational analysis of nucleic acid fragments. 3. The magnitude of torsional angle in d(TpA) from CCOP and HCOP NMR coupling constants. *Nucleic Acids Res. 12*, 5419–5428.
75. Frisch, M. J., Trucks, G. W., Schlegel, H. B., Scuseria, G. E., Robb, M. A., Cheeseman, J. R., Montgomery, J. A., Vreven, T., Kudin, K. N., Burant, J. C., Millam, J. M., Iyengar, S. S., Tomasi, J., Barone, V., Mennucci, B., Cossi, M., Scalmani, G., Rega, N., Petersson, G. A., Nakatsuji, H., Hada, M., Ehara, M., Toyota, K., Fukuda, R., Hasegawa, J., Ishida, M., Nakajima, T., Honda, Y., Kitao, O., Nakai, H., Klene, M., Li, X., Knox, J. E., Hratchian, H. P., Cross, J. B., Adamo, C., Jaramillo, J., Gomperts, R., Stratmann, R. E., Yazyev, O., Austin, A. J., Cammi, R., Pomelli, C., Pomelli, J., Ochterski, W., Ayala, P. Y., Morokuma, K., Voth, G. A., Salvador, P., Dannenberg, J. J., Zakrzewska, V. G., Daniels, A. D., Farkas, O., Rabuck, A. D., Raghavachari, K., and Ortiz, J. V. (2004) GAUSSIAN 03, Gaussian, Inc., Wallingford, CT.
76. Kouchakdjian, M., Marinelli, E., Gao, X., Johnson, F., Grollman, A., and Patel, D. (1989) NMR studies of exocyclic 1,N^2-propanodeoxyguanosine adducts (X) opposite purines in DNA duplexes: Protonated X(*syn*):A(*anti*) pairing (acidic pH) and X(*syn*):G(*anti*) pairing (neutral pH) at the lesion site. *Biochemistry 28*, 5647–5657.
77. Arnott, S., and Hukins, D. W. L. (1972) Optimised parameters for A-DNA and B-DNA. *Biochem. Biophys. Res. Commun. 47*, 1504–1509.
78. Case, D. A., Pearlman, D. A., Caldwell, J. W., Cheatham, T. E., III, Wang, J., Ross, W. S., Simmerling, C. L., Darden, T. A., Merz, K. M., Stanton, R. V., Cheng, A. L., Vincent, J. J., Crowley, M., Tsui, V., Gohlke, H., Radmer, R. J., Duan, Y., Pitera, J., Massova, I., Seibel, G. L., Singh, U. C., Weiner, P. K., and Kollman, P. A. (2002) AMBER, version 7.0, University of California, San Francisco.
79. Hawkins, G. D., Cramer, C. J., and Truhlar, D. G. (1995) Pairwise solute descreeing of solute charges from a dielectric medium. *Chem. Phys. Lett. 246*, 122–129.
80. Hawkins, G. D., Cramer, C. J., and Truhlar, D. G. (1996) Parametrized models of aqueous free energies of solvation based on pairwise descreening of solute atomic charges from a dielectric medium. *J. Phys. Chem. 100*, 19824–19839.
81. Tsui, V., and Case, D. A. (2000) Theory and applications of the generalized Born solvation model in macromolecular simulations. *Biopolymers 56*, 275–291.
82. Ryckaert, J.-P., Ciccotti, G., and Berendsen, H. J. C. (1977) Numerical integration of the cartesian equations of motion of a system with constraints: Molecular dynamics of n-alkanes. *J. Comput. Phys. 23*, 327–341.
83. Liu, Y., Zhao, D., Altman, R., and Jardetzky, O. (1992) A systematic comparison of three structure determination methods from NMR data: Dependence upon quality and quantity of data. *J. Biomol. NMR 2*, 373–388.
84. Thomas, P. D., Basus, V. J., and James, T. L. (1991) Protein solution structure determination using distances from two-dimensional nuclear Overhauser effect experiments: Effect of approximations on the accuracy of derived structures. *Proc. Natl. Acad. Sci. U.S.A. 88*, 1237–1241.
85. Lu, X. J., and Olson, W. K. (2003) 3DNA: A software package for the analysis, rebuilding and visualization of three-dimensional nucleic acid structures. *Nucleic Acids Res. 31*, 5108–5121.
86. de los Santos, C., Zaliznyak, T., and Johnson, F. (2001) NMR characterization of a DNA duplex containing the major acrolein-derived deoxyguanosine adduct γ-OH-1,-N^2-propano-2′-deoxyguanosine. *J. Biol. Chem. 276*, 9077–9082.
87. Patel, D. J., Shapiro, L., and Hare, D. (1987) DNA and RNA: NMR studies of conformations and dynamics in solution. *Q. Rev. Biophys. 20*, 35–112.
88. Reid, B. R. (1987) Sequence-specific assignments and their use in NMR studies of DNA structure. *Q. Rev. Biophys. 20*, 2–28.
89. Boelens, R., Scheek, R. M., Dijkstra, K., and Kaptein, R. (1985) Sequential assignment of imino- and amino-proton resonances in ^{1}H NMR spectra of oligonucleotides by two-dimensional NMR spectroscopy. Application to a *lac* operator fragment. *J. Magn. Reson. 62*, 378–386.
90. Cho, Y. J., Wang, H., Kozekov, I. D., Kozekova, A., Kurtz, A. J., Jacob, J., Voehler, M., Smith, J., Harris, T. M., Rizzo, C. J., Lloyd, R. S., and Stone, M. P. (2006) Orientation of the crotonaldehyde-derived N^2-[3-Oxo-1*S*-methyl-propyl]-dG DNA adduct hinders

interstrand cross-link formation in the 5′-CpG-3′ sequence. *Chem. Res. Toxicol. 19*, 1019–1029.

91. Cho, Y. J., Kozekov, I. D., Harris, T. M., Rizzo, C. J., and Stone, M. P. (2007) Stereochemistry modulates the stability of reduced interstrand cross-links arising from *R*- and *S*-α-CH_3-γ-OH-1,N^2-propano-2′-deoxyguanosine in the 5′-CpG-3′ DNA sequence. *Biochemistry 46*, 2608–2621.
92. Ruan, Q., Kim, H. Y., Jiang, H., Penning, T. M., Harvey, R. G., and Blair, I. A. (2006) Quantification of benzo[a]pyrene diol epoxide DNA-adducts by stable isotope dilution liquid chromatography/tandem mass spectrometry. *Rapid Commun. Mass Spectrom. 20*, 1369–1380.
93. Stout, M. D., Jeong, Y. C., Boysen, G., Li, Y., Sangaiah, R., Ball, L. M., Gold, A., and Swenberg, J. A. (2006) LC/MS/MS method for the quantitation of *trans*-2-hexenal-derived exocyclic 1,N^2-propanodeoxyguanosine in DNA. *Chem. Res. Toxicol. 19*, 563–570.
94. Zhang, S., Villalta, P. W., Wang, M., and Hecht, S. S. (2006) Analysis of crotonaldehyde- and acetaldehyde-derived 1,N^2-propanodeoxyguanosine adducts in DNA from human tissues using liquid chromatography electrospray ionization tandem mass spectrometry. *Chem. Res. Toxicol. 19*, 1386–1392.
95. Goodenough, A. K., Schut, H. A., and Turesky, R. J. (2007) Novel LC-ESI/MS/MS_n method for the characterization and quantification of 2′-deoxyguanosine adducts of the dietary carcinogen 2-amino-1-methyl-6-phenylimidazo[4,5-b]pyridine by 2-D linear quadrupole ion trap mass spectrometry. *Chem. Res. Toxicol. 20*, 263–276.
96. Zayas, B., Stillwell, S. W., Wishnok, J. S., Trudel, L. J., Skipper, P., Yu, M. C., Tannenbaum, S. R., and Wogan, G. N. (2007) Detection and quantification of 4-ABP adducts in DNA from bladder cancer patients. *Carcinogenesis 28*, 342–349.

BI8011143